Design and Testing of Gust Load Alleviation Control Laws for the IAWTM Wind Tunnel Test

Christopher J. Forte*
KBR Wyle, Inc., Moffett Field, CA 94035

Nhan T. Nguyen†
NASA Ames Research Center, Moffett Field, CA 94035

John F. Quindlen‡
Boeing Technology Innovation, Huntington Beach, CA, 92647

Heather S. Hussain§
Boeing Technology Innovation, Charlotte, NC, 28202

This paper summarizes the design and testing of gust load alleviation (GLA) control laws developed for the Integrated Adaptive Wing Technology Maturation (IAWTM) wind tunnel test campaign at NASA's Langley Research Center Transonic Dynamics Tunnel (TDT). The IAWTM program is a joint NASA and Boeing effort to demonstrate and validate control and sensing technologies necessary to enable higher aspect ratio flexible transport aircraft. Two of the primary drivers of wing structural sizing in a flexible, high aspect ratio wing are the maneuver and gust loads experienced by the aircraft in the flight envelope. Gust load alleviation control laws aim to reduce the gust loads experienced by the aircraft in flight in order to minimize the required wing structure, reduce fatigue associated with larger gust loads, and improve passenger ride quality. As part of the IAWTM program, multiple GLA control laws were developed by NASA and Boeing and tested in the TDT. One of the designs utilizes gust measurement devices positioned upstream of the test article in the TDT to act as a surrogate LIDAR for a forward-looking feedforward controller. The second control law is a multi-objective linear quadratic Gaussian design with the objective of minimizing wing root strain, which utilizes the onboard accelerometer and strain gage sensors for estimation and feedback. NASA also developed a third Hamiltonian-based control law. The designs for the controllers are presented and the wind tunnel results for the June 2025 tests are summarized All three controllers demonstrates a reduction in inboard strain at different gust frequencies.

I. Introduction

The Integrated Adaptive Wing Technology Maturation (IAWTM) program is a multi-year collaborative effort between Boeing and NASA to develop and test technologies that would enable higher aspect ratio commercial transport aircraft. The IAWTM program developed a higher aspect ratio version[1, 2] of the NASA Common Research Model (CRM) [3]. The nominal CRM has an aspect ratio of 9 while the work conducted under the IAWTM program increased the aspect ratio to 13.5. This new model, dubbed the "CRM13", is intended to represent a further evolution in the trend towards conventional higher aspect ratio wings coupled with lighter aircraft structure. Earlier work [2, 4] developed a nominal, full-scale CRM13 aircraft with accompanying simulation model and control laws. The culmination of this effort is a pair of wind tunnel tests conducted at NASA's Langley Research Center Transonic Dynamics Tunnel (TDT) in 2024 and 2025. A dynamically-scaled, half-span wind tunnel model based upon the CRM13 configuration was designed and built for use in the TDT. This model is equipped with a suite of sensors and distributed control surfaces intended for real-time control. Figure 1 pictures the model in the wind tunnel prior to the first entry.

*Aerospace Engineer, Intelligent System Division, Member AIAA.
†Senior Research Scientist, Technical Group Lead, Intelligent Systems Division, Associate Fellow AIAA.
‡GNC Engineer, Guidance, Navigation, Control & Autonomy, Member AIAA.
§Associate Technical Fellow, Guidance, Navigation, Control & Autonomy, Member AIAA.

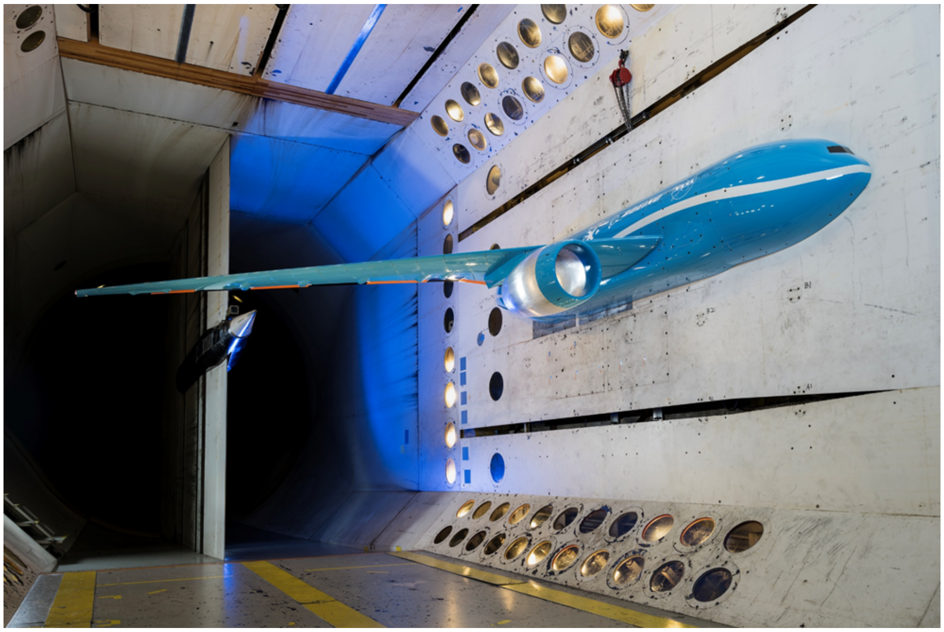

Fig. 1 IAWTM wind tunnel model within NASA's Langley Research Center Transonic Dynamics Tunnel.

One of the primary considerations during the design of high aspect ratio, flexible wings is the structure required to handle the aeroservoelastic loads. In particular, maneuver and gust loads experienced by the aircraft across the flight envelope are the main factors that drive wing structural sizing. As active maneuver load alleviation has reduced the magnitude of the maneuver loads experienced by an aircraft, gust loads have become an increasing concern. Gust load alleviation (GLA) uses active controls to suppress the gust loads experienced by the aircraft during flight, which in turn would help reduce the amount of required wing structure, lessen gust-induced structural fatigue, and even improve passenger ride quality. Gust load alleviation control laws have been an area of active research with a variety of proposed controllers[5–7].

One emerging development is the emergence of light detection and ranging (LIDAR) sensors for use on aircraft[8, 9]. These LIDAR sensors essentially monitor a point in space a set distance in front of the aircraft and detect changes in the local wind field before the aircraft encounters this wind field. Some recent studies have coupled gust load alleviation control laws with these new LIDAR sensors for predictive control architectures[8–11].

Under the IAWTM effort, both Boeing and NASA have developed multiple GLA control laws that were tested during the second wind tunnel entry in 2025. These controllers utilize special upstream sensors in the TDT that acts as a surrogate LIDAR and allows for testing of predictive control schemes. One of the controllers tested tested is a feedforward control law specifically designed to exploit the surrogate LIDAR sensor in order to minimize inboard wing strains. A second controller features a multi-objective linear quadratic Gaussian (LQG) controller that couples the surrogate LIDAR with the onboard feedback sensors. NASA developed a third Hamiltonian-based GLA control law. All three of these controllers were implemented and tested in the TDT and all demonstrated reductions in inboard wing strains. This paper will provide further details on the control system designs and summarize the wind tunnel results.

II. Wind-Tunnel Test Overview

The following section will provide an overview of the NASA Transonic Dynamics Tunnel and the IAWTM wind tunnel model. More detailed information on both topics is found in [2] and [12].

A. Transonic Dynamics Tunnel

The NASA Transonic Dynamics Tunnel (TDT) is a closed-circuit wind tunnel with a 16 × 16 foot test section, capable of using heavy gas (R134a). With regards to IAWTM testing, the use of heavy gas allows the wind tunnel model to be tested at or near nominal cruise Mach and dynamic pressures for a commercial transport aircraft. A top-view of the TDT layout is shown in Figure 2.

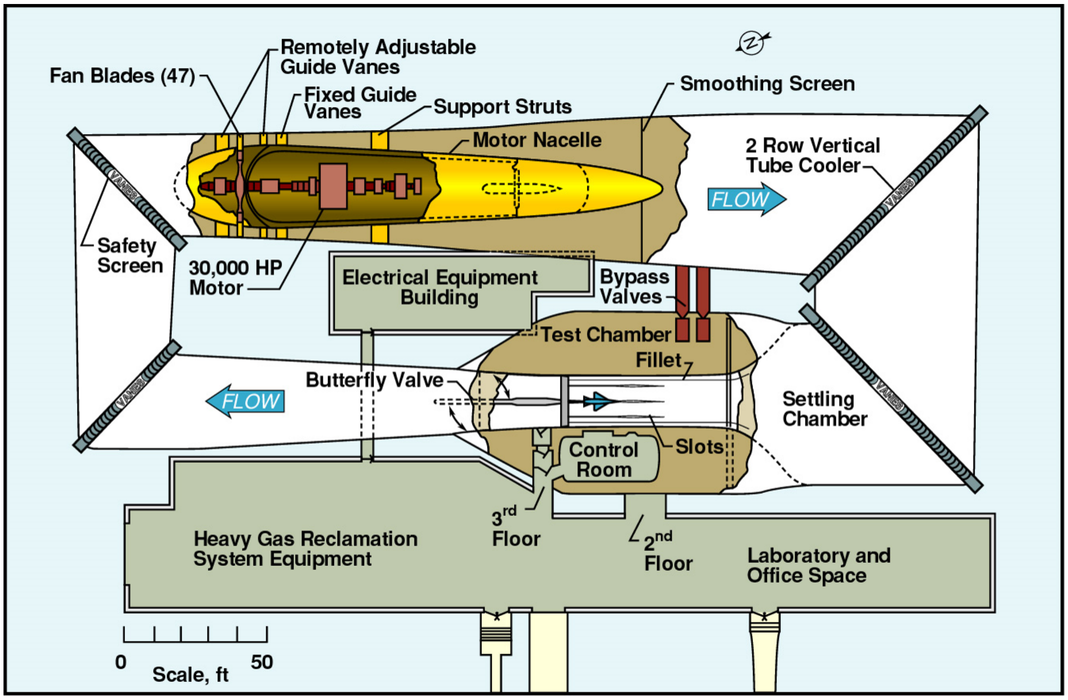

Fig. 2 Top-view of the Transonic Dynamics Tunnel.

The TDT has a niche capability which is critical to the gust load alleviation testing: the upstream airstream oscillation system (AOS) vanes. As shown in Figure 3, there are four vanes located upstream of the model that are used to produce flow changes along the model. There are two pairs of vanes, one on the east wall and one on the west wall. The two surfaces in each pair are mechanically linked, so that they oscillate in-phase at the same frequency and are incapable of being actuated out-of-phase. The two pairs of vanes can oscillate either completely in-phase or out-of-phase, but both pairs oscillated in-phase for the IAWTM gust configuration testing.

The TDT also includes a "gust sniffer" probe that measures the gust response in the front of the test section. The gust sniffer sits in the middle of the test section and is used to simulate a forward-looking sensor, such as a LIDAR. Figure 4 illustrates the positioning of the gust vanes and sniffer in relation to the wind tunnel model. The gust sniffer measurements allow the IAWTM gust load alleviation control laws to demonstrate predictive controllers that exploit the LIDAR-like behavior.

The NASA LaRC TDT Test Facility also includes additional sensors that are used during gust load alleviation. There are sensors that record real-time measurements of Mach, dynamic pressure, and Angle of Attack that will be used by the closed-loop control systems. Additionally, the second IAWTM test entry when the GLA controllers were tested included a laser displacement sensor. This sensor used fiducial markings on the bottom of the outboard wingtip to measure wingtip displacement. These laser displacement measurements have emerged as useful metrics for evaluating GLA controller performance.

B. Wind Tunnel Model

The IAWTM wind tunnel test article is a half-span model of the nominal CRM13 airframe. Figure 5 illustrates the wind tunnel model and highlights some of the major components. Note that the wing is dynamically scaled, but the fuselage has been shortened due to physical size limitations of the wind tunnel. The wing also has a flow-thru nacelle to model the impact of the nacelle weight and inertia on the wing structural dynamics.

As noted in Figure 5, the wind tunnel model is equipped with 10 control surfaces. Seven of these surfaces are electric mini-plain flaps (MPFs) that are controlled via servos located in the wing structure. The remaining 3 surfaces are hydraulically powered ailerons. The hydraulic ailerons are more capable control surfaces with higher bandwidth, but it was infeasible to fit hydraulic lines for all 10 surfaces within the limited space of the wing. The gust load alleviation

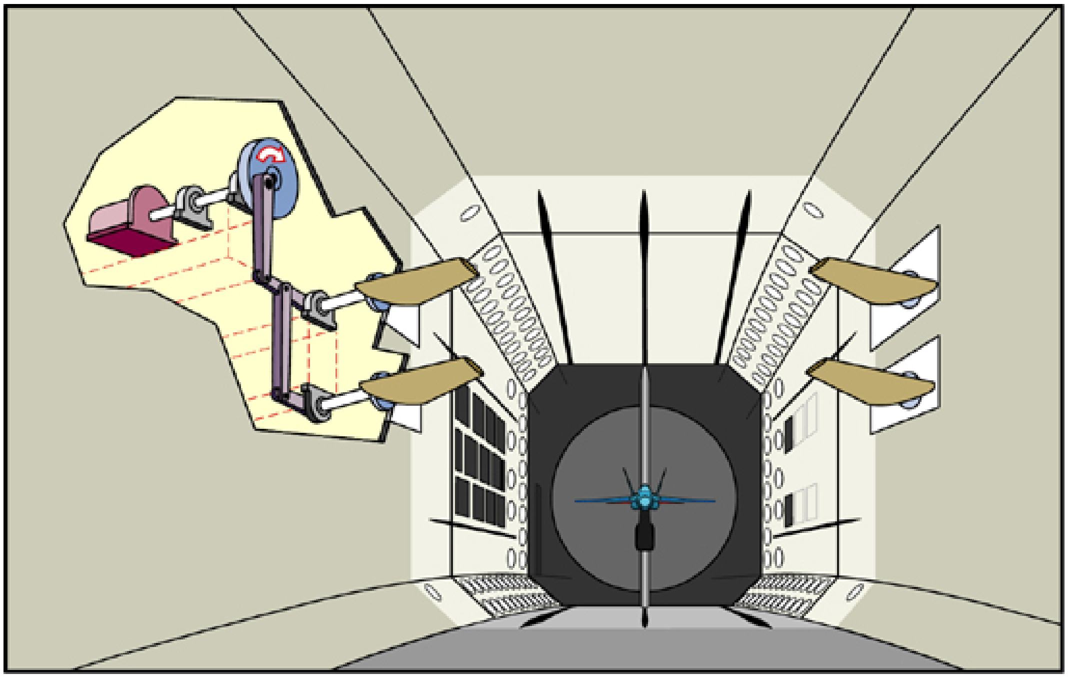

Fig. 3 TDT airstream oscillation system (AOS) vanes.

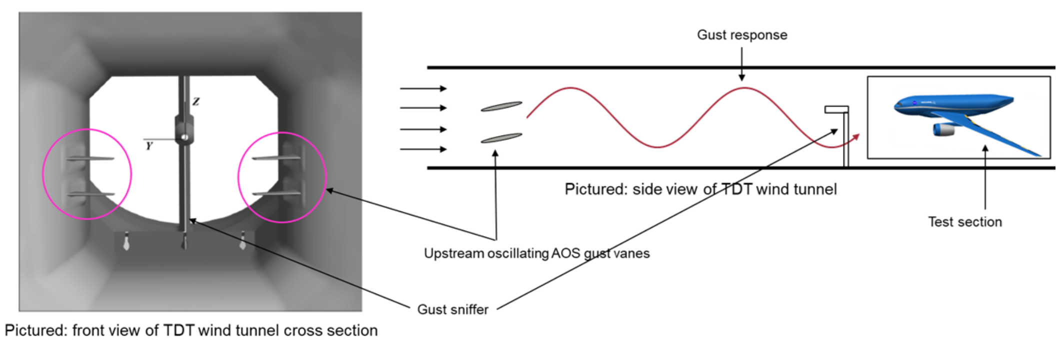

Fig. 4 Positioning of the AOS vanes in relation to the gust sniffer and IAWTM model.

controllers will only utilize the 3 hydraulic ailerons. Figure 6 illustrates the layout of the control surfaces and the nomenclature used for each. The "AILA", "AILB", and "AILC" surfaces are the 3 hydraulic ailerons.

The hydraulically-powered ailerons all have deflection limits of ±10° at the heavy-gas test conditions of interest. The ailerons are physically capable of moving to ±20°, but they have only been approved to operate to ±10° within the pre-test documentation. The electric servo-powered control surfaces have different deflection limits based upon each surface's size and loading, but these surfaces were not used for closed-loop gust load alleviation testing.

In addition to the test equipment provided by the NASA LaRC TDT Test Facility, the IAWTM model is equipped with an integrated suite of different sensors for closed-loop control and monitoring of the wind tunnel model. For gust load alleviation testing, the primary sensors of interest are the 16 one- and three-axis accelerometers and 10 strain gage pairs.

The accelerometer locations and nomenclature are shown in Figure 7. There are three 3-axis accelerometers located on the model: one on the engine nacelle, one where the engine pylon meets the wing, and one at the leading-edge of the spar out at the wingtip. The remaining accelerometers are all single-axis models spread along the wing. Two of these 1-axis accelerometers are aligned in the x-axis to measure fore-aft bending while the rest are all oriented along the z-axis to measure vertical bending. The majority of the wing-based accelerometers are located on the leading-edge of the spar, but a few of the accelerometers oriented in the z-axis were placed on the trailing-edge of the spar to give

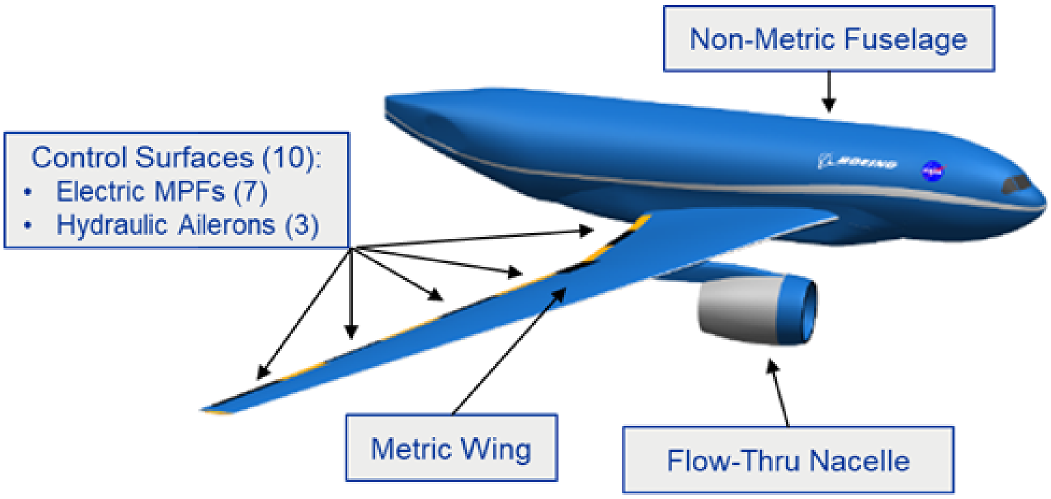

Fig. 5 IAWTM wind tunnel model and major subcomponents.

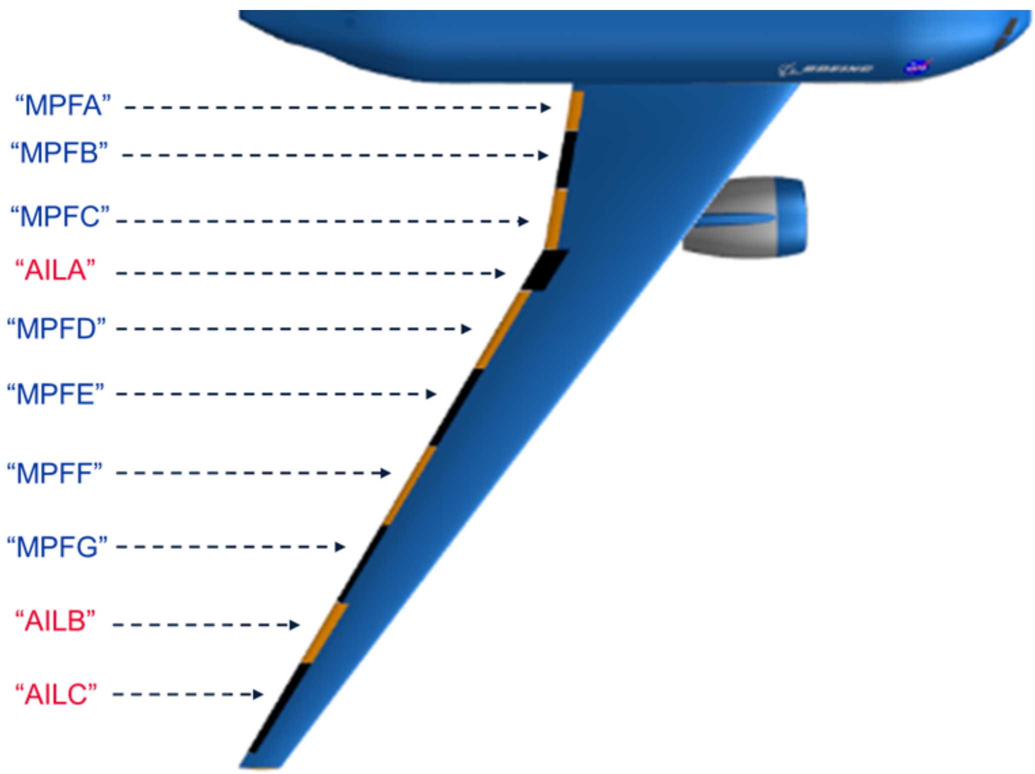

Fig. 6 Layout of the IAWTM wind control surfaces.

indications of wing torsion.

The IAWTM model also has 10 strain gage pairs distributed along the span of the wing. These strain gage pair locations are illustrated in Figure 8. The strain gage pairs consist of 2 gages placed at the same X and Y location on the upper and lower surface of the wing spar. There were flat mounting pads machined into the wing spar to ensure the strain gages were placed at the desired location. For gust load alleviation testing, the primary objective is to minimize wing root bending moment; however, that measurement is not available for real-time monitoring or control. Instead, the inboard-most strain gage, SG01, is used as the surrogate for evaluating controller performance as it is closest to the wing

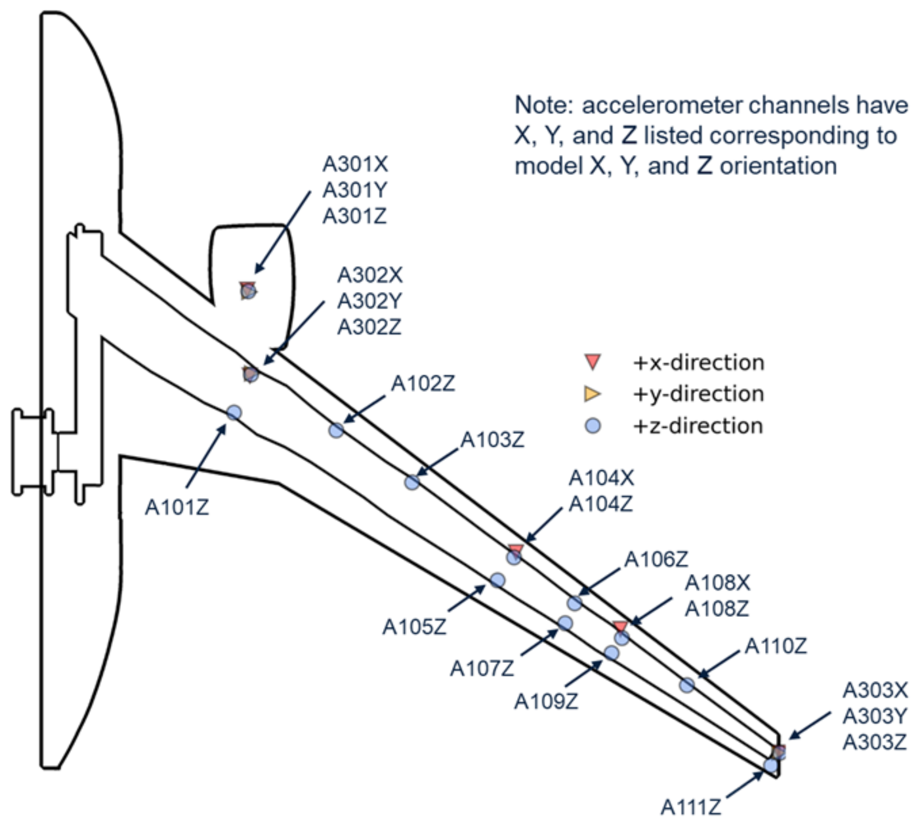

Fig. 7 Locations of the accelerometers on the IAWTM wind tunnel model.

root.

III. Aeroservoelastic Modeling

There has been extensive work by both NASA and Boeing to generate models of the aeroservoelastic (ASE) dynamics of the IAWTM test article[13–17]. NASA has developed ASE models using several different approaches including: rational function approximations using ZAERO, unsteady vortex lattice method using VSPAERO, linearized frequency domain using FUN3D, and reduced order modeling using FUN3D. Ultimately, the ZAERO method has been used to generate the state-space models for control law development.

While the overarching IAWTM test campaigns explored three different boundary condition configurations [2, 12], only the shim-on, ballast-off ("S1B0") configuration was used for gust characterization and gust load alleviation testing. In order to correlate the ASE models with experimental data, NASA and Boeing performed 3 major ground vibration tests (GVTs) and multiple smaller hardware tests in the TDT facility. The data acquired during these GVT activities was used to make several updates to the as-built finite element model (FEM). Table 1 compares the frequency matching and cross-orthogonality of the latest FEM ("AWT6.0") and the latest GVT ("GVT3") conducted immediately prior to the first IAWTM wind tunnel entry in July 2024.

The GVT-correlated FEM (AWT6.0) was used to construct state space models of the S1B0 configuration over the entire test envelope. Table 2 lists the first 5 aeroelastic modes for the target flight conditions used in gust characterization testing. Unsurprisingly, the first wing vertical bending mode shows the most change as a function of flight condition. NASA also computed the predicted flutter boundary for the S1B0 configuration using the ASE models. NASTRAN predicted that flutter would not occur below 500 psf for any flight conditions in the test envelope below Mach 0.7. The predicted flutter boundary is sufficiently far enough from the GLA test conditions that flutter is not a concern in this configuration.

The ASE models cover a grid of flight conditions covering Mach numbers between 0.3 to 0.95 and dynamic pressures between 50 and 300 psf. The ASE model for each flight condition includes 152 outputs, 45 inputs, and 290 states. The

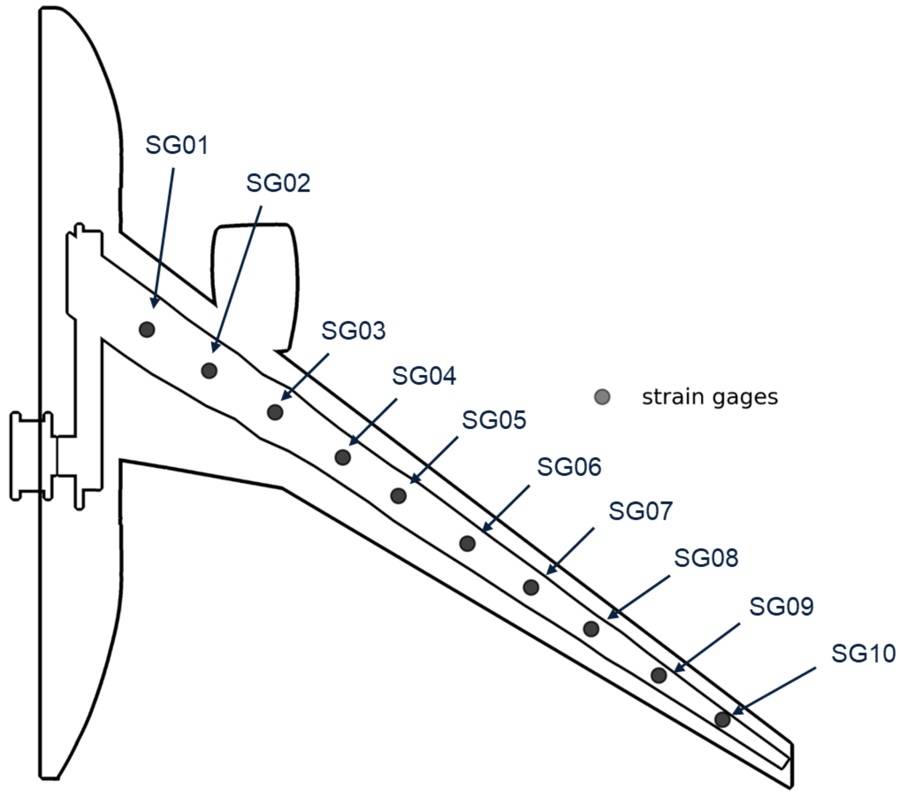

Fig. 8 Locations of strain gage pairs on the IAWTM wind tunnel model.

Table 1 Summary of IAWTM WT test article FEM flexible modes for the shims-on, ballast-off ("S1B0") configuration in the TDT test section compared against the experimental data collected in the latest GVT ("GVT3").

Index	Test f (Hz)	FEM f (Hz)	Error (%)	Cross-Orthogonality	Description
1	3.65	3.67	0.6%	1.00	Wing 1st Vertical Bending
2	8.92	8.90	-0.2%	0.99	Wing 1st Fore-Aft Bending
3	9.70	9.62	-0.9%	0.99	Vehicle Pitch
4	12.09	12.23	1.1%	0.99	Wing 2nd Vertical Bending
5	15.03	14.85	-1.2%	0.97	Wing 2nd Fore-Aft Bending
6	19.60	19.96	1.9%	0.93	Nacelle Side Bending
7	20.07	21.45	6.9%	0.99	Vehicle Pitch + Nacelle Pitch
8	26.24	27.40	4.4%	0.86	Wing 3rd Vertical Bending + Fuselage Pitch
9	27.44	27.40	-0.1%	0.86	Wing 3rd Vertical Bending + Fuselage Yaw
10	27.95	27.94	0.0%	0.91	Wing 3rd Vertical Bending + Fuselage Pitch
11	42.67	43.56	2.1%	0.93	Wing 4th Vertical Bending
12	47.55	47.45	-0.2%	0.93	Wing 1st Torsion

ASE model states correspond to displacement and rate of the first 20 aeroelastic modes and 12 aero lag modeling states for each of those modes. It also includes 10 gust modeling states. The ASE model inputs include position, rate, and acceleration for the 10 control surfaces, as well as position, rate, and acceleration of the TDT pitch angle. Alongside the control surface and TDT pitch angle, the ASE model inputs also include position, rate, and acceleration for each of

Table 2 Change in aeroservoelastic modes with flight condition for the S1B0 model configuration.

Mach	Dynamic Pressure psf	Wing 1st Vert. Bending Hz	Wing 1st Fore-Aft Bending Hz	Vehicle Pitch Hz	Wing 2nd Vert. Bending Hz	Wing 2nd Fore-Aft Bending Hz
AWT6.0 FEM		3.67	8.90	9.62	12.23	14.85
0.3	50	4.23	8.01	8.82	12.05	14.37
0.4	60	4.36	8.01	8.82	12.12	14.37
0.45	65	4.47	8.01	8.81	12.15	14.37
0.5	90	4.75	8.01	8.80	12.24	14.37
0.55	110	5.03	8.01	8.88	12.33	14.37
0.6	126	5.33	8.01	8.77	12.42	14.37
0.65	145	5.51	8.01	8.76	12.47	14.37
0.7	156	5.86	8.01	8.75	12.58	14.37

the 4 gust vanes. These ASE model inputs capture the aeroelastic effects upon the model caused by moving the gust vanes. NASA performed additional analysis in order to characterize the gust vane dynamics with as much accuracy as possible[18]. Figure 9 illustrates the modeling of the gust vane inputs within the ZAERO. The ASE model outputs correspond to sensor measurements such as the accelerometers and strain gages, among a few other signals. The ASE model outputs also include a single variable for the gust sniffer position measurement.

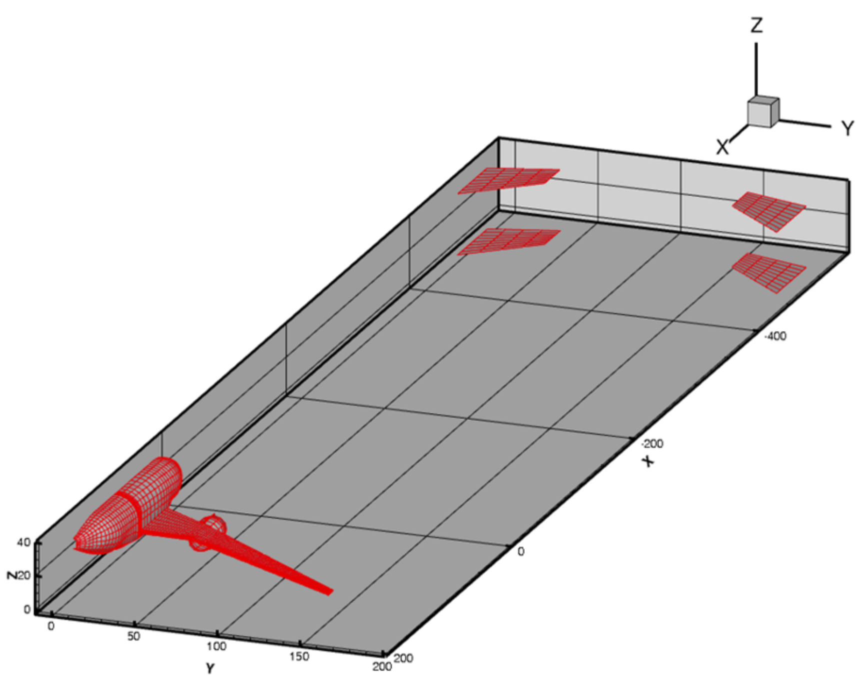

Fig. 9 TDT gust vanes modeled within ZAERO.

As mentioned in Section II.A, each gust vane pair is mechanically linked to oscillate together. For IAWTM gust load alleviation testing, the two pairs of vanes oscillate in-phase together; therefore, the gust vane dynamics are the same for all 4 gust vanes. The gust vane dynamics are modeled as a sinusoidal response controlled by an amplitude (θ_v^{amp}) and frequency (ω_v^{cmd}), shown below in Equation 1.

$$\theta_v(t) = \theta_v^{amp} \sin(\omega_v^{cmd} t + \theta_0) \tag{1}$$

The amplitude of the oscillations is variable, but is mechanically set prior to the test and is inaccessible once heavy gas is pumped into the tunnel. The gust vane amplitude is set to $\theta_v^{amp} = 3°$ for IAWTM testing, which is the maximum approved AOS vane amplitude for the planned test conditions. The gust vane frequency is also variable, but is controlled through hardware in the TDT control room and can thus be changed during the middle of testing. For IAWTM GLA testing, the gust vane frequency varied between $\omega_v^{cmd} = 0$ Hz (AOS off) and $\omega_v^{cmd} = 4$ Hz. Figures 10 and 11 show the response of the ASE model for Mach 0.55, $\bar{q}_\infty = 110$ psf, which is the nominal test condition for gust load alleviation testing. The model is perturbed with a 0.5 Hz oscillatory gust input applied in-phase to all 4 gust vanes. Figure 10 depicts the change in SG01 measurement given the gust inputs, while Figure 11 shows the corresponding gust sniffer reading. Note the time delay between the gust vane input applied upstream of the wind tunnel model and when that gust is encountered downstream at the model and gust sniffer locations.

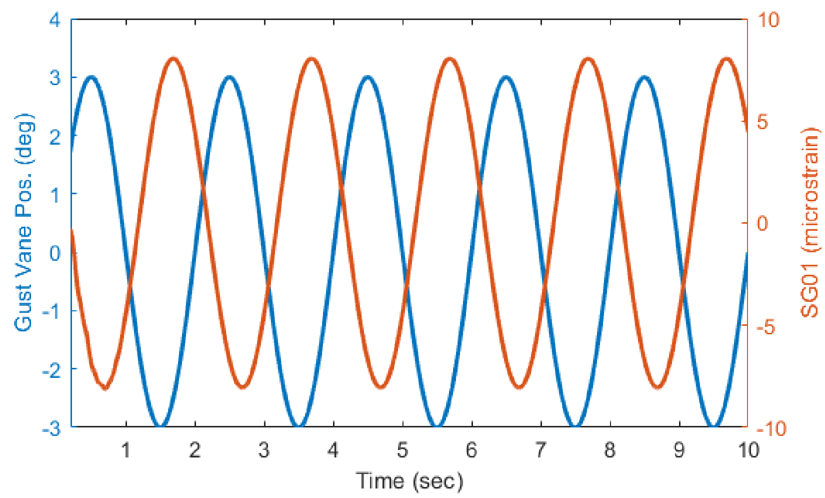

Fig. 10 ASE model output for SG01 given a sinusoidal gust input.

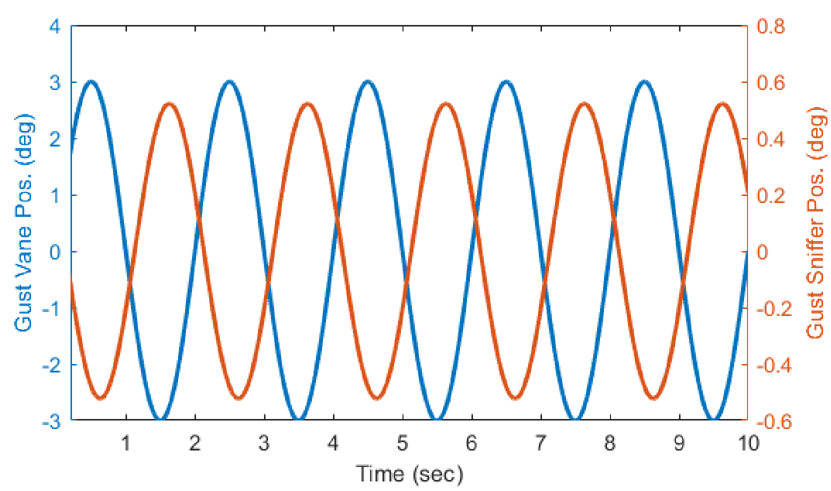

Fig. 11 ASE model output for gust sniffer given a sinusoidal gust input.

Early gust characterization tests during the second wind tunnel entry were performed in order to verify the accuracy of the ASE model's gust response prior to closed-loop gust load alleviation testing. These tests confirmed that the ASE model response matched the experimental data within acceptable tolerances. Figure 12 compares the ASE model's gust sniffer output against the gust sniffer position measurements for a 0.5 Hz gust perturbation at the Mach 0.55, $\bar{q}_\infty = 110$ psf test condition. To generate this comparison, the actual gust vane position measurements from the wind tunnel test were fed into the ASE model. The resulting ASE model gust sniffer output is then compared against the gust sniffer measurements from that same wind tunnel data record. The gust sniffer measurements are noisy, so the figure also includes filtered gust sniffer data after it had been passed through a band-pass filter with a 0.1 Hz lower and 5 Hz higher cutoff frequency. The ASE model prediction closely mirrors the filtered signal. Figure 13 plots some of the strain gage measurements for the same data record. The ASE model does underpredict the magnitude of SG01 when compared against the experimental data, but the phase aligns. The magnitude of other two strain gages, SG03 and SG05, more closely matches.

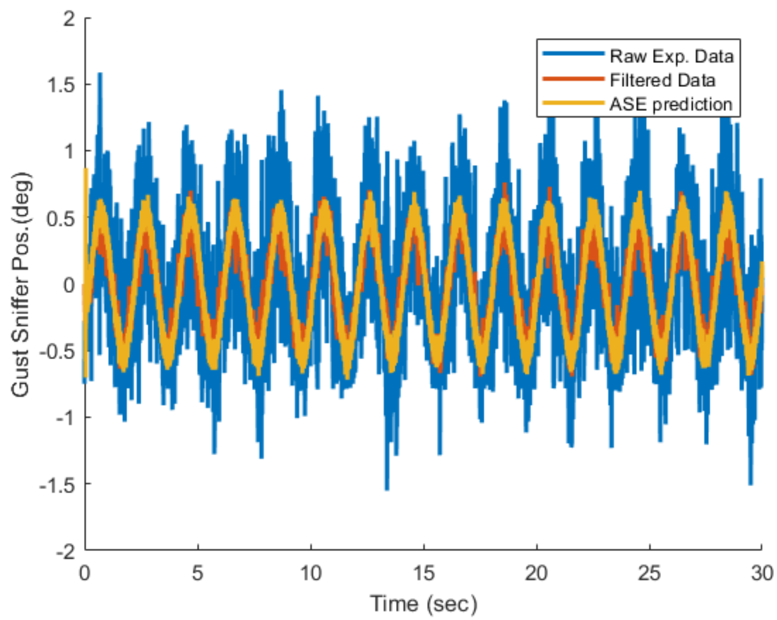

Fig. 12 Comparison of predicted ASE model output for gust sniffer position against raw and filtered experimental data. The ASE model is fed the measured gust vane positions as inputs.

The control surface dynamics were extracted from test data collected during the first wind tunnel entry. The ailerons are modeled as a second-order system with a multiplier and time delay. Experimental results showed the hydraulically-powered aileron dynamics did not vary across the test envelope, unlike what was seen with the electric servo-powered MPFs. The transfer function for the aileron dynamics is shown below in Equation 2. Each surface has different response with the corresponding parameters listed in Table 3.

$$\frac{\delta(s)}{\delta_{cmd}(s)} = K\left(\frac{\omega_n^2}{s^2 + 2\zeta\omega_n s + \omega_n^2}\right)e^{-\tau s} \tag{2}$$

Table 3 Aileron modeling parameters corresponding to Equation 2 for each surface.

Surface	K	ζ	ω_n (rad/sec)	τ (sec)
AILA	0.9792	0.5482	156	0.0027
AILB	1.0760	0.5857	59.055	0.0048
AILC	1.0280	0.3508	195.75	0.0040

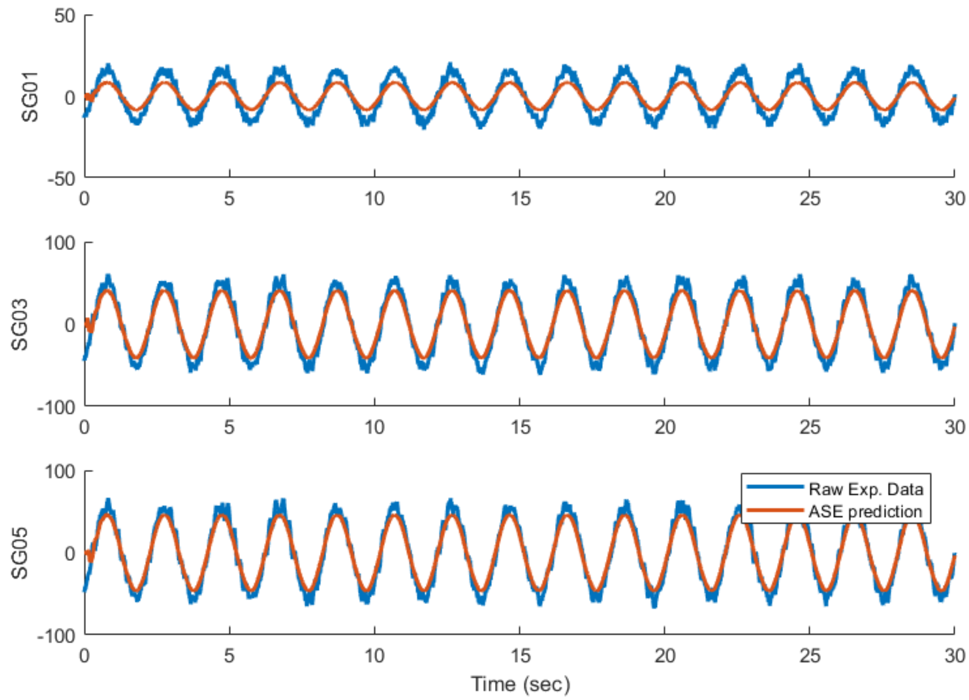

Fig. 13 Comparison of predicted ASE model output for strain gage measurements against raw experimental data. The ASE model is fed the measured gust vane positions as inputs.

IV. Control Law Design

Both Boeing and NASA developed gust load alleviation control laws for the second IAWTM wind tunnel entry in June-July 2025. These control laws were designed to interface with NASA Langley's TDT dSPACE environment for real-time control. All of the Boeing and NASA GLA controllers were also designed with the same objective: minimize inboard-most SG01 measurements. Ideally, the controllers would seek to minimize the wing root bending moment; however, those values are unavailable so strain gage SG01 is used as the closest surrogate. Boeing and NASA utilized noticeably different approaches for GLA, and this section will outline these different controller architectures.

A. Boeing Feedforward Controller

Current research has investigated the use of forward-looking light detection and ranging (LIDAR) sensors installed on aircraft to measure wind velocity a predetermined distance in front of the vehicle[8, 10]. The benefit of such sensors is that wind gusts can be detected before they are encountered by an aircraft and active control can be used to preemptively suppress the impact of those gusts upon ride quality or aeroelastic response. A production-ready gust load alleviation controller could allow for further reduction in structural weight by minimizing peak gust loads and reducing overall gust-induced fatigue on the airframe.

Boeing has developed a feedforward gust load alleviation control system to demonstrate the potential performance improvements of such as system on a LIDAR-equipped aircraft. While it is infeasible to mount a true LIDAR system onboard the IAWTM wind tunnel model, the TDT's gust sniffer sensor provides equivalent forward-looking capability and can be treated as a surrogate LIDAR. Figure 14 provides a general overview of the Boeing GLA control system.

Figure 14 highlights a number of adaptations that are done to explicitly accommodate the TDT test environment that would not be found on a control system for a full-scale aircraft. First, the aeroservoelastic dynamics for the IAWTM wind tunnel model explicitly account the TDT gust vane motion rather than a gust input. As mentioned in Section III, the TDT gust vanes are inputs to the ASE state space models rather than a more general gust perturbation. Accordingly, the Boeing GLA controller design utilizes the gust vane inputs. Similarly, the objective of state estimation has shifted to estimation of the unknown gust vane states. A more detailed depiction of the GLA control system architecture for the

TDT test is shown in Figure 15.

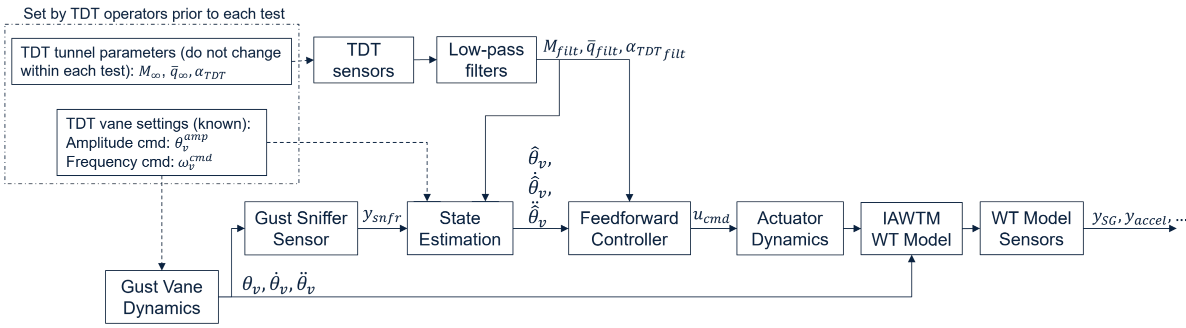

Fig. 14 High-level overview of the Boeing gust load alleviation control system.

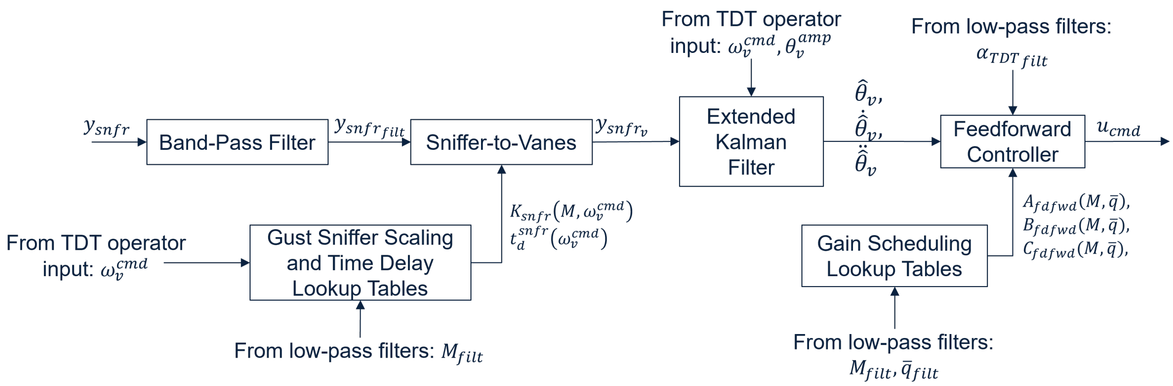

Fig. 15 More detailed depiction of the GLA control system architecture that highlights some of the TDT-specific controller modifications.

1. Gust Vane State Estimation

The first component of the GLA control system is the estimation of the gust vane states. Although the gust vanes follow an oscillatory response with known amplitude (θ_v^{amp}) and frequency (ω_v^{cmd}), the current position of the gust vanes is not known in real-time. Therefore, the gust vane states will need to be estimated based upon the downstream gust sniffer measurements. As a side note, Section V will discuss that measurements of the gust vane position of one of the west-wall AOS vanes are actually available during post-processing, but these measurements are not available to the real-time dSPACE environment where the controllers are implemented for testing. These measurements are used validate the state estimates in post-processing.

The gust vane dynamics in Equation 1 include the known amplitude (θ_v^{amp}) and frequency (ω_v^{cmd}), but the initial phase angle (θ_0) is unknown. Equation 3 rewrites the gust dynamics to include a phase angle (ϕ_{phase}). The objective of state estimation is to estimate this phase angle so it can be used to produce estimated gust vane position ($\hat{\theta}_v$), velocity ($\dot{\hat{\theta}}_v$), and acceleration ($\ddot{\hat{\theta}}_v$).

$$\theta_v(t) = \theta_v^{amp} \sin(\omega_v^{cmd} t + \theta_0) = \theta_v^{amp} \sin\left(\phi_{phase}(t)\right) \tag{3}$$

$$\dot{\theta}_v(t) = \theta_v^{amp} \omega_v^{cmd} \cos\left(\phi_{phase}(t)\right) \tag{4}$$

$$\ddot{\theta}_v(t) = -\theta_v^{amp} \omega_v^{cmd} \omega_v^{cmd} \sin\left(\phi_{phase}(t)\right) \tag{5}$$

As shown in Figure 4, the gust sniffer sits downstream of the AOS vanes and measures the airflow at that location. Thus, the gust sniffer does not explicitly measure the gust vane position, but its downstream effect. The comparison of gust vane and sniffer position in Figure 11 showed that the gust sniffer measurement can be treated as a scaled and shifted signal of the gust vane position. Equation 6 models the gust sniffer measurement with a time-delay (t_d^{snfr}) and scaling parameter (K_{snfr}) applied to the gust vane position (θ_v).

$$y_{snfr}(t) = K_{snfr}\theta_v(t - t_d^{snfr}) \tag{6}$$

The effective time delay and scaling parameters at selected gust frequencies for the primary test condition are shown in Tables 4 and 5. These values were confirmed during open-loop gust characterization tests conducted prior to closed-loop gust load alleviation testing.

Table 4 Effective time delays (t_d^{snfr}) at selected gust vane frequencies for Mach 0.55, $\bar{q}_\infty = 110psf$.

ω_v^{cmd} (Hz)	0.5	1.0	1.5	2.0
t_d^{snfr} (sec)	1.89	0.82	0.50	0.35

Table 5 Effective scaling parameter (K_{snfr}) at selected gust vane frequencies for Mach 0.55, $\bar{q}_\infty = 110psf$.

ω_v^{cmd} (Hz)	0.5	1.0	1.5	2.0
K_{snfr}	0.1730	0.1715	0.1704	0.1689

Equation 7 is the inverse of Equation 6, where the gust sniffer measurements are scaled and shifted to produce a gust vane measurement ($y_v(t)$). As shown in Figure 15, the actual controller implementation sends the gust sniffer measurement through a band-pass filter to attenuate noise. The filter cutoff frequencies were set to 0.1 and 5 Hz since no testing was planned to be conducted outside the 0.5 to 3 Hz range.

$$y_v(t) = K_{snfr}^{-1} y_{snfr}(t + t_d^{snfr}) \tag{7}$$

Due to the known nonlinear dynamics listed in Equations 3 - 5, a discrete-time extended Kalman filter (EKF) was used to estimate the gust vane states. The state vector consists of angular frequency (ω_k) and phase (ϕ_k). Even though (ω_v^{cmd}) is known, estimated ω_k provides extra flexibility in case the achieved angular frequency is slightly different from the hardware command. The state dynamics can be written as a linear equation with an forward Euler approximation, shown below in Equation 8. The measurement equation in Eq. 9 is modeled as the nonlinear sinusoidal response.

$$\begin{aligned} x_{k+1} &= F_k x_k + w_k \\ &= \begin{bmatrix} 1 & 0 \\ \Delta t & 1 \end{bmatrix} \begin{bmatrix} \omega_k \\ \phi_k \end{bmatrix} + w_k \end{aligned} \tag{8}$$

$$y_k = \theta_v^{amp} \sin(\phi_k) + v_k \tag{9}$$

The noise terms w_k, v_k are defined as zero-mean Gaussian distributions: $w_k \sim N(0, Q)$ and $v_k \sim N(0, R)$. Q is modeled as a diagonal matrix with the first element set to 1.6E-4 Hz and the second set to 0.0573°. R is a scalar term with magnitude 6°.

The extended Kalman filter dynamics are described below. The time update equations for the a priori state and covariance estimates are given in Equations 10 and 11. The initial estimate for the state vector is $\hat{x}_{0|0} = [\omega_v^{cmd}, 0]^T$.

$$\hat{x}_{k|k-1} = F_k \hat{x}_{k-1|k-1} \tag{10}$$

$$P_{k|k-1} = F_k P_{k-1|k-1} F_k^T + Q \tag{11}$$

The measurement update dynamics for the posteriori estimates are listed in Equations 12, 13, and 14. The measurement gradient matrix H_k consists of the partial derivative of the measurement equation (Eq. 9) about the current apriori state estimates $\hat{x}_{k|k-1}$, shown in Equation 15. At the conclusion of the measurement update step, the posteriori state estimates are used to compute estimated gust vane position, rate, and acceleration. These are passed to the feedforward controller.

$$K_k = P_{k|k-1} H_k^T (H_k P_{k|k-1} H_k^T + R)^{-1} \tag{12}$$
$$P_{k|k} = (I_{2x2} - K_k H_k) P_{k|k-1} \tag{13}$$
$$\hat{x}_{k|k} = \hat{x}_{k|k-1} + K_k \left(y_k - \theta_v^{amp} \sin(\hat{\phi}_{k|k-1})\right) \tag{14}$$

$$H_k = \left.\frac{\partial y_k}{\partial x}\right|_{\hat{x}_{k|k-1}} = \begin{bmatrix} 0 & \theta_v^{amp} \cos(\hat{\phi}_{k|k-1}) \end{bmatrix} \tag{15}$$

$$\hat{\theta}_v(t_k) = \theta_v^{amp} \sin(\hat{\phi}_{k|k}) \tag{16}$$
$$\dot{\hat{\theta}}_v(t_k) = \theta_v^{amp} \hat{\omega}_{k|k} \cos(\hat{\phi}_{k|k}) \tag{17}$$
$$\ddot{\hat{\theta}}_v(t_k) = -\theta_v^{amp} \hat{\omega}_{k|k} \hat{\omega}_{k|k} \sin(\hat{\phi}_{k|k}) \tag{18}$$

The state estimation was tested in a simulated wind tunnel testing environment that used realistic values for noise extracted from prior characterization testing. Figure 16 shows the simulated performance of the EKF for a 0.5 Hz gust response at Mach 0.55, $\bar{q}_\infty = 110psf$. The estimate of gust vane position closely matches the true gust vane position.

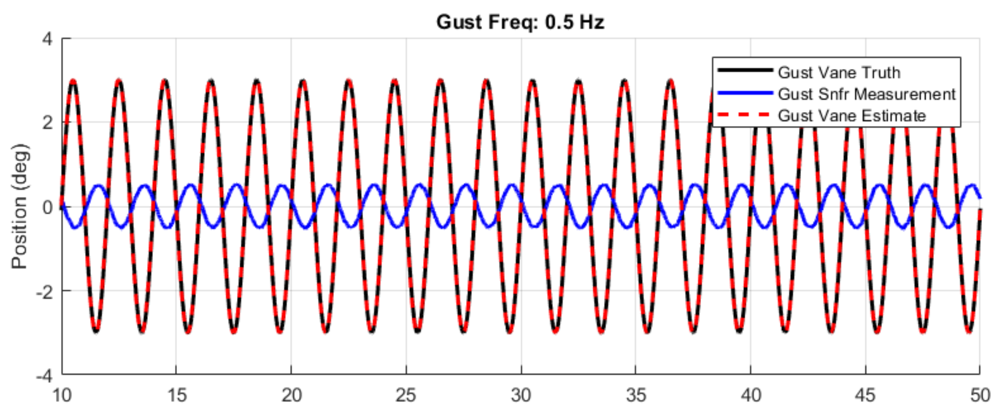

Fig. 16 Simulated Kalman filter performance for a 0.5 Hz gust at Mach 0.55, $\bar{q}_\infty = 110psf$.

2. Feedforward Control Design

A feedforward gust load alleviation controller is designed for each test condition of interest in the wind tunnel test envelope. The controller is designed to minimize strain gage response using the hydraulic ailerons. Equations 19 and 20 list the ASE dynamics used for controller design, where x_f represents the aeroelastic states, u_{ail} contains the position, rate, and acceleration for each of the ailerons, and u_{gust} includes the gust vane position, rate, and acceleration. Since the feedforward controller is designed around the strain gages, only the 10 outputs associated with the strain gages (y_{sg}) are considered.

$$\dot{x}_f = A_f x_f + B_{ail} u_{ail} + B_{gust} u_{gust} \tag{19}$$
$$y_{sg} = C_f x_f + D_{ail} u_{ail} + D_{gust} u_{gust} \tag{20}$$

The aeroelastic dynamics require the position, rate, and acceleration of each control surface. Equations 21 and 22 rewrite the dynamics shown in Equation 2 in state space form. The internal actuator states are given as x_a, while u_{cmd} contains the position command for each aileron. The output u_{ail} is the corresponding position, rate, and acceleration terms used by the ASE dynamics.

$$\dot{x}_a = A_a x_a + B_a u_{cmd} \tag{21}$$
$$u_{ail} = C_a x_a + D_a u_{cmd} \tag{22}$$

The state space dynamics can be written in a combined form as shown below. For the feedforward control system design, it is unnecessary to track all 290 states within x_f. Instead, the controller design process utilizes model reduction on the aeroelastic dynamics to remove aeroelastic modes outside the frequency range of interest. The resulting dynamics are shown in Equations 25 and 26, where $x_{f_{red}}$ is the reduced set of states and $A_{f_{red}}$, $B_{ail_{red}}$, $B_{gust_{red}}$, and $C_{f_{red}}$ are the reduced model equivalents.

$$\begin{bmatrix} \dot{x}_f \\ \dot{x}_a \end{bmatrix} = \begin{bmatrix} A_f & B_{ail}C_a \\ 0 & A_a \end{bmatrix} \begin{bmatrix} x_f \\ x_a \end{bmatrix} + \begin{bmatrix} B_{ail}D_a \\ D_{ail}D_a \end{bmatrix} u_{cmd} + \begin{bmatrix} B_{gust} \\ 0 \end{bmatrix} u_{gust} \tag{23}$$
$$y_{sg} = \begin{bmatrix} C_f & D_{ail}C_a \end{bmatrix} \begin{bmatrix} x_f \\ x_a \end{bmatrix} + D_{ail}D_a u_{cmd} + D_{gust}u_{gust} \tag{24}$$

$$\begin{aligned} \begin{bmatrix} \dot{x}_{f_{red}} \\ \dot{x}_a \end{bmatrix} &= \begin{bmatrix} A_{f_{red}} & B_{ail_{red}}C_a \\ 0 & A_a \end{bmatrix} \begin{bmatrix} x_{f_{red}} \\ x_a \end{bmatrix} + \begin{bmatrix} B_{ail_{red}}D_a \\ D_{ail}D_a \end{bmatrix} u_{cmd} + \begin{bmatrix} B_{gust_{red}} \\ 0 \end{bmatrix} u_{gust} \\ &= \bar{A} \begin{bmatrix} x_{f_{red}} \\ x_a \end{bmatrix} + \bar{B}_{ail}u_{ail} + \bar{B}_{gust}u_{gust} \end{aligned} \tag{25}$$

$$y_{sg} = \begin{bmatrix} C_{f_{red}} & D_{ail}C_a \end{bmatrix} \begin{bmatrix} x_{f_{red}} \\ x_a \end{bmatrix} + D_{ail}D_a u_{cmd} + D_{gust}u_{gust} \tag{26}$$

The feedforward controller gains are designed using the output-weighting linear quadratic regulator (LQR) design process. The LQR controller minimizes the following objective function that places a weighting on the strain gage outputs, y_{sg}.

$$J = \int_0^\infty \left(y_{sg}^T Q_{sg} y_{sg} + u_{cmd}^T R_{cmd} u_{cmd} \right) dt \tag{27}$$

The corresponding control surface commands follow the standard state feedback format.

$$u_{cmd} = -K_{lqr} \begin{bmatrix} x_{f_{red}} \\ x_a \end{bmatrix} \tag{28}$$

The LQR weighting matrices, Q_{sg} and R_{cmd}, are both diagonal matrices. The control penalty, R_{cmd}, places different penalties on the control surface commands. Since the primary objective of the IAWTM gust load alleviation controllers is the minimization of SG01, the output penalty matrix, Q_{sg}, places a high penalty on the first strain gage output, SG01. The penalties for the remaining strain gages rolls off towards zero at SG10. The feedforward controller dynamics combine the closed-loop LQR state feedback response with the gust vane inputs, as shown below. The internal controller state, x_{ctrl}, estimates the response of x_a and $x_{f_{red}}$ and uses it to produce the control surface commands.

$$\dot{x}_{ctrl} = (\bar{A} - \bar{B}_{ail}K_{lqr})x_{ctrl} + \bar{B}_{gust}u_{gust} \tag{29}$$

$$u_{cmd} = -K_{lqr}x_{ctrl} \tag{30}$$

Boeing developed four controllers for testing in the TDT using this process. Due to questionable responses observed during Entry 1 and 2 testing, it was uncertain whether aileron AILB could be used for high bandwidth control. As a result, there were two batches of controllers: one batch that utilized AILB for control while another did not use AILB at all. The system dynamics in Equations 25 and 26 as well as the control penalty matrix R_{cmd} were truncated when AILB was not employed for control. Additionally, there were two versions of controller testing: one version was intended to perform better at lower frequencies while another was intended for improved performance at higher frequencies with potential degradation at lower frequencies. The four controllers are summarized below.

- **Controller 1A:** lower frequency performance, aileron AILB engaged
- **Controller 1B:** lower frequency performance, aileron AILB disengaged
- **Controller 2A:** higher frequency performance, aileron AILB engaged
- **Controller 2B:** higher frequency performance, aileron AILB disengaged

These four controllers were tested in the simulation environment prior to Entry 2. These tests predicted that the controllers would reduce the strain gage SG01 measurements in their intended frequency range of interest. Figures 17 and 18 illustrate the simulated response of Controllers 1A and 1B at Mach 0.55, $\bar{q}_\infty$ = 110 psf for a 0.5 Hz gust vane excitation against the simulated open-loop response. Note that the strain gage sensor models include zero-mean Gaussian noise levels extracted from prior Entry 1 data records at that test condition. The simulated Controller 1A response shows a 45.2% reduction in SG01 root mean square (RMS) while the simulated Controller 1B response shows a 28.1% reduction in SG01 RMS without the use of aileron AILB.

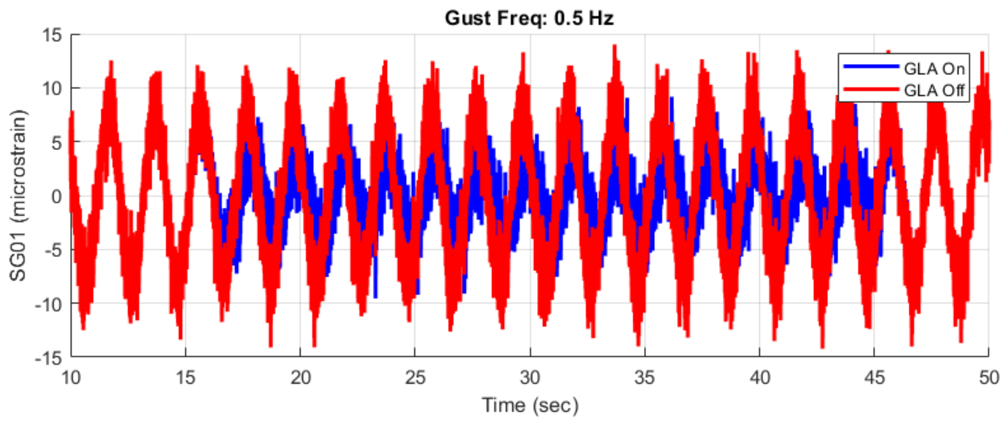

Fig. 17 Simulated results for Controller 1A at Mach 0.55, $\bar{q}_\infty$ = 110 psf given a 0.5 Hz gust vane excitation. The results show a 45.2% reduction in the SG01 root mean square (RMS) when compared against the simulated open-loop response.

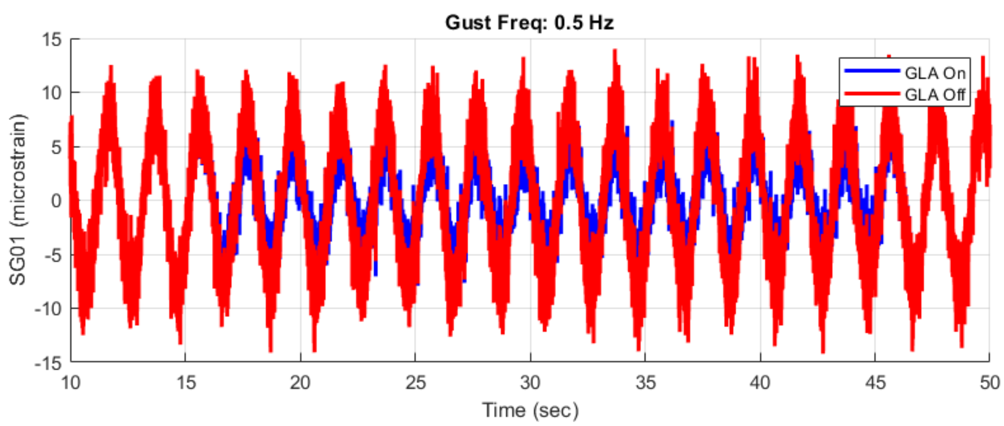

Fig. 18 Simulated results for Controller 1B at Mach 0.55, $\bar{q}_\infty$ = 110 psf given a 0.5 Hz gust vane excitation. The results show a 28.1% reduction in the SG01 root mean square (RMS) when compared against the simulated open-loop response.

B. NASA Ames Multi-Objective Linear Quadratic Gaussian Controller

The multi-objective optimal control approach offers strong potential for structural load alleviation [19–21]. In this study, the LQG control strategy provides a practical evaluation of this concept, employing a cost function that extends the standard LQR formulation with an additional weighting on the root strain output, and combining it with a Kalman filter for state estimation.

1. ASE Model Reduction

The ASE model contains hundreds of states, which is excessive for practical control design and motivates model reduction. During GLA testing, the model is excited by gust vanes oscillating sinusoidally at a single frequency, ω_g. Model reduction is performed under the assumption that the steady-state response is sinusoidal at a single frequency. For GLA control, the reduced model assumes a steady-state response at the gust frequency, ω_g. The ASE model is given by:

$$\begin{bmatrix} \dot{x}_s \\ \dot{x}_l \\ \dot{x}_f \end{bmatrix} = \begin{bmatrix} A_{ss} & A_{sl} & 0 \\ A_{ls} & A_{ll} & 0 \\ A_{fs} & A_{fl} & A_{ff} \end{bmatrix} \begin{bmatrix} x_s \\ x_l \\ x_f \end{bmatrix} + \begin{bmatrix} B_{sa} \\ B_{la} \\ B_{fa} \end{bmatrix} x_a + \begin{bmatrix} E_{sw} \\ E_{lw} \\ E_{fw} \end{bmatrix} w \tag{31}$$

$$y = \begin{bmatrix} C_s & C_l & C_f \end{bmatrix} \begin{bmatrix} x_s \\ x_l \\ x_f \end{bmatrix} + D_a x_a + F_w w \tag{32}$$

$$x_s = \begin{bmatrix} q \\ \dot{q} \end{bmatrix} \tag{33}$$

$$x_a = \begin{bmatrix} \delta \\ \dot{\delta} \\ \ddot{\delta} \end{bmatrix} \tag{34}$$

$$w = \begin{bmatrix} \theta_g \\ \dot{\theta}_g \end{bmatrix} \tag{35}$$

The structural state vector x_s contains the generalized structural displacement vector q and the generalized rate vector $\dot{q}$ for the first 20 structural modes. The aerodynamic lag state vector x_l includes 12 lag states per structural mode, while the anti-aliasing filter state vector x_f contains 4 states per output. The model also includes the gust disturbance vector w. The actuator state vector x_a consists of the actuator position δ, rate $\dot{\delta}$, and acceleration $\ddot{\delta}$.

The lag state dynamics are given by:

$$\dot{x}_l = A_{ll} x_l + A_{ls} x_s + B_{la} x_a + E_{lw} w \tag{36}$$

Upon expansion the following is obtained:

$$\dot{x}_l = A_{ll} x_l + A_{lq} q + A_{l\dot{q}} \dot{q} + B_{l\delta} \delta + B_{l\dot{\delta}} \dot{\delta} + B_{l\ddot{\delta}} \ddot{\delta} + E_{l\theta_g} \theta_g + E_{l\dot{\theta}_g} \dot{\theta}_g \tag{37}$$

Using the single frequency sinusoidal steady-state response the following is assumed:

$$x_l = a_1 \sin \omega_g t + a_2 \cos \omega_g t \tag{38}$$

$$q = b_1 \sin \omega_g t + b_2 \cos \omega_g t \tag{39}$$

$$\delta = c_1 \sin \omega_g t + c_2 \cos \omega_g t \tag{40}$$

$$x_g = d_1 \sin \omega_g t + d_2 \cos \omega_g t \tag{41}$$

Substituting, Eqs. 38-41 into 37 gives:

$$\begin{aligned} \dot{x}_l(t) &= a_1 \omega_g \cos \omega_g t - a_2 \omega_g \sin \omega_g t \\ &= A_{ll} \left(a_1 \sin \omega_g t + a_2 \cos \omega_g t \right) + A_{lq} \left(b_1 \sin \omega_g t + b_2 \cos \omega_g t \right) \\ &\quad + A_{l\dot{q}} \left(b_1 \omega_g \cos \omega_g t - b_2 \omega_g \sin \omega_g t \right) + B_{l\delta} \left(c_1 \sin \omega_g t + c_2 \cos \omega_g t \right) \\ &\quad + B_{l\dot{\delta}} \left(c_1 \omega_g \cos \omega_g t - c_2 \omega_g \sin \omega_g t \right) - B_{l\ddot{\delta}} \left(c_1 \omega_g^2 \sin \omega_g t + c_2 \omega_g^2 \cos \omega_g t \right) \\ &\quad + E_{l\theta_g} \left(d_1 \sin \omega_g t + d_2 \cos \omega_g t \right) + E_{l\dot{\theta}_g} \left(d_1 \omega_g \cos \omega_g t - d_2 \omega_g \sin \omega_g t \right) \end{aligned} \tag{42}$$

By grouping like terms and solving for a_1 and a_2, the equation for the lag state and its derivative is obtained[22], which is given by:

$$x_l = K_1 x_s + K_2 x_a + K_3 w \tag{43}$$

$$\dot{x}_l = K_1 K_g x_s + K_2 K_{g_a} x_a + K_3 K_{g_w} w \tag{44}$$

Eqs. 43 and 44 are then substituted into the lag state equation given by Eq. 36, yielding:

$$\dot{x}_l = K_1 K_g x_s + K_2 K_{g_a} x_a + K_3 K_{g_w} w = A_{ll}(K_1 x_s + K_2 x_a + K_3 w) + A_{ls} x_s + B_{la} x_a + E_{lw} w \tag{45}$$

By comparing like terms, the resulting Sylvester equations are obtained from which K_1, K_2, and K_3 can be solved:

$$K_1 K_g - A_{ll} K_1 = A_{ls} \tag{46}$$

$$K_2 K_{g_a} - A_{ll} K_2 = B_{la} \tag{47}$$

$$K_3 K_{g_w} - A_{ll} K_3 = E_{lw} \tag{48}$$

Eq. 43 is substituted into the ASE system in Eqs. 31 and 32, thereby removing the lag states. The reduced system is given by:

$$\begin{bmatrix} \dot{x}_s \\ \dot{x}_f \end{bmatrix} = \begin{bmatrix} A_{ss} + A_{sl} K_1 & 0 \\ A_{fs} + A_{fl} K_2 & A_{ff} \end{bmatrix} \begin{bmatrix} x_s \\ x_f \end{bmatrix} + \begin{bmatrix} B_{sa} + A_{sl} K_2 \\ B_{fa} + A_{fl} K_1 \end{bmatrix} x_a + \begin{bmatrix} E_{sw} + A_{sl} K_3 \\ E_{fw} + A_{fl} K_3 \end{bmatrix} w \tag{49}$$

$$y = \begin{bmatrix} C_s + C_l K_1 & C_f \end{bmatrix} \begin{bmatrix} x_s \\ x_f \end{bmatrix} + (D_a + C_l K_2) x_a + (F_w + C_l K_3) w \tag{50}$$

The same approach is utilized to further reduce the anti-aliasing filter states. Then, the state x_s is partitioned into the x_b which is the state vector for the first 10 structural modes and x_h which is the state vector for the remaining 10 structural modes. The state vector for the high frequency modes x_h is also removed using the same method.

The reduced system is then combined with the actuator dynamics. A second order Butterworth low-pass filter with cutoff frequency of 10 Hz is applied to the command to eliminate high-frequency contents in the control signal. The 10 Hz cutoff frequency is chosen because the ASE model accuracy decreases at frequencies beyond this bandwidth when comparing the response of the ASE model to the test data acquired by the system identification experiment. The reduced order system used for control design is assembled [22], given by:

$$\dot{x}(t) = Ax(t) + Bu(t) + Ew(t) \tag{51}$$

$$y(t) = Cx(t) + Fw(t) \tag{52}$$

where

$$x(t) = \begin{bmatrix} x_b(t) \\ x_{act}(t) \\ x_{f_l}(t) \end{bmatrix} \tag{53}$$

The state vector x now contains only the state vector for the first 10 structural modes x_b, the actuator state vector x_{act}, and low-pass filter state vector x_{f_l}. For full details on the model reduction process see Ref. [22].

2. *Gust Disturbance Modeling*

The gust vane dynamics are modeled in as follows:

$$\dot{x}_v(t) = A_v x_v(t) + B_v u_v(t) \tag{54}$$

where $u_v(t)$ is the commanded gust vane position and $x_v(t)$ is the vector containing the gust vane position $\theta_v(t)$, the gust vane velocity $\dot{\theta}_v(t)$, and the gust vane acceleration $\ddot{\theta}_v(t)$ which is given by:

$$x_v(t) = \begin{bmatrix} \theta_v(t) \\ \dot{\theta}_v(t) \\ \ddot{\theta}_v(t) \end{bmatrix} \tag{55}$$

This can be expressed in transfer function form:

$$X_v(s) = G_1(s)U_v(s) \tag{56}$$

$$G_1(s) = (sI - A_v)^{-1}B_v \tag{57}$$

The output of the gust vane model contains the gust vane position and velocity and is expressed as:

$$y_v(t) = C_v x_v(t) \tag{58}$$

where

$$C_v = \begin{bmatrix} 1 & 0 & 0 \\ 0 & 1 & 0 \end{bmatrix} \tag{59}$$

The disturbance state $w(t)$ represents the gust vane position and velocity delayed by the convective time delay between the gust vanes and the model which is given by:

$$w(t) = y_v(t - t_d) \tag{60}$$

The gust vanes move sinusoidally at a known frequency ω_g and amplitude θ_0. Thus, $\theta_g(t)$ written as:

$$\theta_g(t) = \theta_0 \sin(\omega_g t + \phi) \tag{61}$$

The dynamics for gust disturbance $w(t)$ can therefore be written as:

$$\dot{w}(t) = A_w w(t) \tag{62}$$

where

$$A_w = \begin{bmatrix} 0 & 1 \\ -\omega_g^2 & 0 \end{bmatrix} \tag{63}$$

3. Multi-Objective Optimal Control

The optimal control is derived using the following multi-objective cost function:

$$J = \lim_{t_f \to \infty} \frac{1}{2} \int_0^{t_f} [x^\top(t)Qx(t) + u^\top(t)Ru(t) + M^\top(t)Q_M M(t)]\, dt \tag{64}$$

The last term in the integral is an addition to the standard LQR cost function and penalizes the response in the wing-root strain sensor. The wing-root strain sensor output is given by

$$M(t) = M_x x(t) + M_w w(t) \tag{65}$$

The optimal control is given by:

$$u(t) = -R^{-1}B^\top[Sx(t) + Pw(t)] = -K_x x(t) + K_w w(t) \tag{66}$$

where

$$K_x = R^{-1}B^\top S \tag{67}$$

$$K_w = -R^{-1}B^\top P \tag{68}$$

The matrices S and P are computed by solving the following modified Riccati equation:

$$SA + A^\top S - SBR^{-1}B^\top S + \bar{Q} = 0 \tag{69}$$

and the Sylvester equation:

$$(A^\top - SBR^{-1}B^\top)P + PA_w + Q_w = 0 \tag{70}$$

where

$$\bar{Q} = Q + M_x^\top Q_M M_x \tag{71}$$

$$Q_w = M_x^\top Q_M M_x + SE \tag{72}$$

4. Estimation

Two approaches are utilized for state and gust estimation. The first employs an extended-state Kalman filter and the second utilizes the upstream gust sniffer to estimate the disturbance. The states in Eqs. 51 and 52 are extended using the disturbance dynamics given in Eq. 62:

$$x_e(t) = A_e x_e(t) + B_e u(t) \tag{73}$$

$$y(t) = C_e x_e(t) \tag{74}$$

where

$$x_e(t) = \begin{bmatrix} x(t) \\ w(t) \end{bmatrix} \tag{75}$$

$$A_e = \begin{bmatrix} A & E \\ 0 & A_w \end{bmatrix} \tag{76}$$

$$B_e = \begin{bmatrix} B \\ 0 \end{bmatrix} \tag{77}$$

$$C_e = \begin{bmatrix} C & F \end{bmatrix} \tag{78}$$

The Kalman filter gain L_k is computed utilizing the sensor noise covariance information and a process noise model[22]. The equation for the extended-state Kalman filter is given by:

$$\dot{\hat{x}}_e = A_e \hat{x}_e(t) + B_e u(t) + L_k[y(t) - C_e \hat{x}_e(t)] \tag{79}$$

Note that $\hat{x}_e$ contains both state and gust estimates that feed into the control law. This method uses onboard accelerometers and strain gauges (without the gust sniffer). Inboard strain gauges and outboard accelerometers are considered for the Kalman filter sensor set. An extensive search is performed to determine the candidate sensor set that provides robust stability margins and a primary sensor set consisting of A111z, A104z, SG01, and SG03 is chosen[22].

In contrast, the second approach incorporates the upstream gust sniffer as a preview measurement to support reconstruction of the gust state. The gust sniffer is mounted upstream of the model and measures the local flow angle. Its dynamics are modeled as:

$$\dot{x}_{sn}(t) = A_{sn}\, x_{sn}(t) + B_{sn}\, x_v(t - t_g), \tag{80}$$

$$y_{sn}(t) = C_{sn}\, x_{sn}(t), \tag{81}$$

or equivalently in the Laplace domain:

$$Y_{sn}(s) = G_2(s)\, X_v(s)\, e^{-st_g}, \tag{82}$$

where

$$G_2(s) = C_{sn}(sI - A_{sn})^{-1}B_{sn}. \tag{83}$$

Because the gust sniffer measurement contains sensor noise, two filtering techniques are employed. The first uses a Kalman filter based on a sinusoidal model of the flow angle measured by the gust sniffer at the gust frequency ω_g:

$$\dot{x}_{snf}(t) = A_{snf}\, x_{snf}(t) \tag{84}$$

$$y_{sn}(t) = C_{snf}\, x_{snf}(t) \tag{85}$$

where

$$A_{snf} = \begin{bmatrix} 0 & 1 \\ -\omega_g^2 & 0 \end{bmatrix}, \tag{86}$$

$$x_{snf}(t) = \begin{bmatrix} \theta_{sn}(t) \\ \dot{\theta}_{sn}(t) \end{bmatrix} \tag{87}$$

$$C_{snf} = \begin{bmatrix} 1 & 0 \end{bmatrix} \tag{88}$$

Let L_{snf} denote the Kalman filter gain. The resulting estimator dynamics are:

$$\dot{\hat{x}}_{snf}(t) = A_{snf}\hat{x}_{snf}(t) + L_{snf}\left[y_{sn}(t) - C_{snf}\hat{x}_{snf}(t)\right] \tag{89}$$

with transfer-function representation:

$$\hat{Y}_{sn,f}(s) = G_{3_k}(s)Y_{sn}(s) \tag{90}$$

where

$$G_{3_k}(s) = C_{snf}(sI - A_{snf} + L_{snf}C_{snf})^{-1}L_{snf} \tag{91}$$

A conventional low-pass filter is also used for noise reduction. An eight-pole Butterworth low-pass filter with a 4.5 Hz cutoff frequency is employed. The cutoff is chosen to be marginally higher than the maximum planned gust-excitation frequency of 4 Hz, thereby attenuating noise while retaining the relevant gust content. Its dynamics are expressed as:

$$Y_{sn,f}(s) = G_{3_{lp}}(s)Y_{sn}(s). \tag{92}$$

The overall relationship between the gust vane command $U_v(s)$ and the filtered sensor output $\hat{Y}_{sn,f}(s)$ is:

$$\begin{aligned} \hat{Y}_{sn,f}(s) &= G_3(s)G_2(s)G_1(s)U_v(s)e^{-st_g} \\ &= G(s)U_v(s)e^{-st_g} \end{aligned} \tag{93}$$

where $G(s) = G_3(s)G_2(s)G_1(s)$ represents the transfer function of the combined system without the delay. Note that when utilizing the Kalman filter for gust sniffer noise filtering $G_3(s) = G_{3_k}(s)$ and $G_3(s) = G_{3_{lp}}(s)$ when the low-pass filter is used. For a sinusoidal vane command $u_v(t) = u_v \cos \omega_g t$ the filtered sniffer output is:

$$\hat{y}_{sn,f}(t) = |G(j\omega_g)|u_v\left(t + \frac{\angle G(j\omega_g)}{\omega_g} - t_g\right) \tag{94}$$

Hence the gust vane position command can be recovered as:

$$u_v(t) = \frac{1}{|G(j\omega_g)|}\hat{y}_{sn,f}\left(t - \frac{\angle G(j\omega_g)}{\omega_g} + t_g\right) \tag{95}$$

With $u_v(t)$ it is then possible to compute $x_v(t)$ using Eq. 54. Then the $x_v(t)$ is delayed by t_d which is the convective time delay between the gust vanes and the model which provides $w(t)$. Because the gust vane states are not directly measured but reconstructed from the filtered sensor output using the known transfer functions and delay compensations, the resulting signals represent the estimated gust quantities. A Kalman filter is also utilized in the second scheme for state estimation, although the state is not extended and the gust estimate from the sniffer estimation is treated as an known input to the Kalman filter. This system is given by:

$$\dot{\hat{x}}(t) = A\hat{x}(t) + Bu(t) - L[y(t) - (C\hat{x}(t) + F\hat{w}(t))] + E\hat{w}(t) \tag{96}$$

The two estimation methods represent distinct approaches to gust and state estimation. The extended-state Kalman filter provides onboard estimation of both structural states and gust disturbances using local sensor feedback, making it suitable for closed-loop control when upstream measurements are unavailable. In contrast, the gust sniffer-based approach provides a preview estimate of the incoming gust field based on measured flow angularity and known system dynamics, enabling feedforward control. Further details on the LQG GLA approach can be found in Ref. [22].

C. NASA Ames Hamiltonian Controller

The Hamiltonian controller developed by Nguyen [23] is based on Hamilton's principle for distributed control of infinite-dimensional Lagrangian systems governed by partial differential equations. This control framework employs operator theory to model Lagrangian systems. The structural dynamics of a flexible structure can be expressed as the following Lagrangian system in linear operator form:

$$m(x)\frac{\partial^2 w(x,t)}{\partial t^2} + Lw(x,t) = f\left(w(x,t), \frac{\partial w(x,t)}{\partial t}, u(x,t)\right) + e(x)g(t) \tag{97}$$

The distributed mass is $m(x)$ and L is a self-adjoint linear operator given by:

$$L = m^{-1}(x)\sum_{i=0}^{m}(-1)^i \frac{\partial^i}{\partial x^i}\left(k_i(x)\frac{\partial^i}{\partial x^i}\right) \tag{98}$$

The distributed displacement is $w(x,t)$ and is expressed as the product between the eigenfunction $\phi(x)$ and the generalized displacement $q(t)$:

$$w(x,t) = \phi(x)q(t) \tag{99}$$

The Hamiltonian function then provides the framework for representing the total energy of a flexible structure and for analyzing its dynamic behavior under control and aerodynamic forces. It therefore can be used to analyze the closed-loop structural dynamics under aerodynamic forces[23–25]. In this case, the ASE system is cast as a structural dynamic model, where the generalized mass and stiffness matrices capture the dominant structural modes. Here, the Hamiltonian approach is used to derive the gust load alleviation control design, providing conditions for dissipativity that inform gain selection and closed-loop performance. The structural dynamics of the system is expressed in the general form as:

$$M\ddot{q}(t) + Kq(t) = F_q q(t) + F_{\dot{q}}\dot{q}(t) + F_\delta \delta(t) + F_{\dot{\delta}}\dot{\delta}(t) + F_{\ddot{\delta}}\ddot{\delta}(t) + F_w w(t) \tag{100}$$

The right-hand side of the equation represents the generalized forces acting on the structure. Assuming that the control input $\delta(t)$ exhibits harmonic behavior at a single frequency ω_g, the acceleration term of the control input can be approximated as $\ddot{\delta}(t) \approx -\omega_g^2\delta(t)$, which reduces the structural dynamics to

$$M\ddot{q}(t) + Kq(t) = F_q q(t) + F_{\dot{q}}\dot{q}(t) + (F_\delta - F_{\ddot{\delta}}\omega_g^2)\delta(t) + F_{\dot{\delta}}\dot{\delta}(t) + F_w w(t) \tag{101}$$

The control action is defined by a state-feedback law:

$$\delta_c(t) = -K_q q(t) - K_{\dot{q}}\dot{q}(t) - K_w w(t) \tag{102}$$

whose time derivative is given by:

$$\dot{\delta}_c(t) = -K_q \dot{q}(t) - K_{\dot{q}}\ddot{q}(t) - K_w \dot{w}(t) \tag{103}$$

The disturbance evolves according to $\dot{w}(t) = A_w w(t)$, therefore:

$$\dot{\delta}_c(t) = -K_q \dot{q}(t) - K_{\dot{q}}\ddot{q}(t) - K_w A_w w(t) \tag{104}$$

To assess system stability, the Hamiltonian is defined as:

$$H = \frac{1}{2}\dot{q}^\top(t)M\dot{q}(t) + \frac{1}{2}q^\top(t)Kq(t) \tag{105}$$

whose time derivative is:

$$\begin{aligned}
\dot{H} &= \dot{q}^\top(t)\, M\ddot{q}(t) + \dot{q}^\top(t)\, Kq(t) && (106)\\
&= \dot{q}^\top(t)[M\ddot{q}(t) + Kq(t)] && (107)\\
&= \dot{q}^\top(t)\left[F_q q(t) + F_{\dot{q}}\dot{q}(t) + (F_\delta - F_{\ddot{\delta}}\omega_g^2)\,\delta_c(t) + F_{\dot{\delta}}\dot{\delta}_c(t) + F_w w(t)\right] && (108)
\end{aligned}$$

The conditions for dissipativity are imposed as:

$$\Delta\dot{H}_q = \dot{q}^\top(t)[F_q - (F_\delta - F_{\ddot{\delta}}\omega_g^2)K_q]q(t) \le 0 \tag{109}$$

$$\Delta \dot{H}_{\dot{q}} = \dot{q}^\top(t)[F_{\dot{q}} - (F_\delta - F_{\ddot{\delta}}\omega_g^2)K_{\dot{q}} - F_{\dot{\delta}}K_q]\dot{q}(t) \leq 0 \tag{110}$$

$$\Delta \dot{H}_{\ddot{q}} = \dot{q}^\top(t)[-F_{\dot{\delta}}K_{\dot{q}}]\ddot{q}(t) \leq 0 \tag{111}$$

These inequalities ensure that the rate change of stored system energy remains non-positive, guaranteeing dissipativity. The gain K_q is determined by setting $\Delta\dot{H}_q$ to zero which gives:

$$F_q - (F_\delta - F_{\ddot{\delta}}\omega_g^2)K_q = 0 \tag{112}$$

The pseudo-inverse method is used to solve for K_q which results in:

$$K_q = [(F_\delta - F_{\ddot{\delta}}\omega_g^2)^\top(F_\delta - F_{\ddot{\delta}}\omega_g^2)]^{-1}(F_\delta - F_{\ddot{\delta}}\omega_g^2)^\top F_q \tag{113}$$

To determine $K_{\dot{q}}$, $\Delta\dot{H}_{\dot{q}}$ is set to a negative definite quantity which is chosen to be $-2\zeta\omega_n$ which gives:

$$F_{\dot{q}} - (F_\delta - F_{\ddot{\delta}}\omega_g^2)K_{\dot{q}} - F_{\dot{\delta}}K_q = -2\zeta\omega_n \tag{114}$$

where ω_n are the modal frequencies and ζ are the prescribed damping ratios. The pseudo-inverse method is used to solve for $K_{\dot{q}}$ which results in:

$$K_{\dot{q}} = [(F_\delta - F_{\ddot{\delta}}\omega_g^2)^\top(F_\delta - F_{\ddot{\delta}}\omega_g^2)]^{-1}(F_\delta - F_{\ddot{\delta}}\omega_g^2)^\top(F_{\dot{q}} - F_{\dot{\delta}}K_q + 2\zeta\omega_n) \tag{115}$$

A damping ratio of $1/\sqrt{2}$ is chosen as an initial damping ratio for each mode, which is then tuned between damping ratios of 0.28 and 0.71, focusing on the most active modes. Eq. 111 represents the apparent mass contribution to the system. This means the $K_{\dot{q}}$ must be sufficiently small so the apparent mass remains positive definite.

To determine the gain K_w, the control command in Eq. 102 is substituted into Eq. 101. Isolating the terms involving the disturbance $w(t)$ setting them to zero yields:

$$-(F_\delta - F_{\ddot{\delta}}\omega_g^2)K_w w(t) - F_{\dot{\delta}}K_w\dot{w}(t) + F_w w(t) = 0 \tag{116}$$

Since the disturbance evolves according to Eq. 62, therefore:

$$-(F_\delta - F_{\ddot{\delta}}\omega_g^2)K_w w(t) - F_{\dot{\delta}}K_w A_w w(t) + F_w w(t) = 0 \tag{117}$$

Thus, the following Sylvester equation is obtained from which K_w is obtained:

$$-(F_\delta - F_{\ddot{\delta}}\omega_g^2)K_w - F_{\dot{\delta}}K_w A_w + F_w = 0 \tag{118}$$

The feedback gains K_q and $K_{\dot{q}}$ can be expressed as:

$$\delta_c(t) = -K_q\, q(t) - K_{\dot{q}}\, \dot{q}(t) - K_w\, w(t) \tag{119}$$

$$= -K_{x_b}\, x_b(t) - K_w w(t) \tag{120}$$

where

$$K_{x_b} = \begin{bmatrix} K_q & K_{\dot{q}} \end{bmatrix} \tag{121}$$

The Hamiltonian gains provide a control command $\delta_c(t)$ but not the actuator input $u(t)$ directly. To achieve command tracking, a linear quadratic integral (LQI) control strategy is implemented. The control position $\delta(t)$ is given by:

$$\delta(t) = C_\delta x(t) \tag{122}$$

The integral error is defined by:

$$\begin{aligned} e(t) &= \int_0^\tau \left[\delta_c(t) - \delta(t)\right] d\tau \\ &= \int_0^\tau \left[\delta_c(t) - C_\delta x(t)\right] d\tau \end{aligned} \tag{123}$$

The time derivative of the integral error is given by:

$$\dot{e}(t) = \delta_c(t) - C_\delta x(t) \tag{124}$$

The system is extended to include the integral error which gives:

$$\dot{\bar{x}}(t) = \bar{A}\bar{x}(t) + \bar{B}u(t) + \bar{E}w(t) + V\delta_c(t) \tag{125}$$

where

$$\bar{x}(t) = \begin{bmatrix} x(t) \\ e(t) \end{bmatrix} \tag{126}$$

$$\bar{A} = \begin{bmatrix} A & 0 \\ -C_\delta & 0 \end{bmatrix} \tag{127}$$

$$\bar{B} = \begin{bmatrix} B \\ 0 \end{bmatrix} \tag{128}$$

$$V = \begin{bmatrix} 0 \\ I \end{bmatrix} \tag{129}$$

The control command is then expressed in terms of $\bar{x}(t)$:

$$\delta_c(t) = -K_{x_b}\, x_b(t) - K_w\, w(t) \tag{130}$$

$$= -K_{\bar{x}}\, \bar{x}(t) - K_w\, w(t) \tag{131}$$

where

$$K_{\bar{x}} = \begin{bmatrix} K_{x_b} & 0 \end{bmatrix} \tag{132}$$

The LQI control minimizes the cost function given by:

$$J = \frac{1}{2}\int_0^\infty [\bar{x}^\top(t)Q\bar{x}(t) + u^\top(t)Ru(t)]dt \tag{133}$$

The optimal control is given by:

$$u = -\tilde{K}_{\bar{x}}\bar{x} + \tilde{K}_w w \tag{134}$$

where

$$\tilde{K}_{\bar{x}} = R^{-1}\bar{B}^\top S \tag{135}$$

$$\tilde{K}_w = -R^{-1}\bar{B}^\top T \tag{136}$$

The matrices S and T are computed by solving the following Riccati Equation

$$S\tilde{A} + \tilde{A}^\top - S\bar{B}R^{-1}\bar{B}^\top S + Q = 0 \tag{137}$$

and the Sylvester equation

$$(\tilde{A}^\top - S\bar{B}R^{-1}\bar{B}^\top)T + TA_w = SVK_w \tag{138}$$

where

$$\tilde{A} = \bar{A} - VK_{\bar{x}} \tag{139}$$

Note that $x(t)$ and $w(t)$ are not available and therefore estimated via techniques outlined in Sec. IV.B.4. Full details on Hamiltonian control approach can be found in Ref. [26].

V. Test Results

The NASA and Boeing gust load alleviation control laws and their variants were tested in the TDT as part of the IAWTM test campaign. The following subsections summarize the execution of the GLA controllers and their corresponding results.

A. Boeing Results

Each of the 4 Boeing controllers were tested during IAWTM Entry 2. Despite pre-test intentions to conduct gust load alleviation testing at different test conditions, there was only time to conduct GLA testing at the primary Mach 0.55, $\bar{q}_{\infty}$ = 110 psf test point. During testing, NASA added a laser displacement sensor at the wingtip that provided measurements of wingtip movement. Although there was no equivalent of this sensor in the ASE models and thus it cannot be explicitly used in the controller design state, the laser displacement sensor was found to be a good secondary metric of controller performance.

Figure 19 shows the extended Kalman filter's performance given a 0.5 Hz perturbation of the gust vanes at the test condition. As mentioned previously, the actual position of the west wall gust vanes can be obtained in post-processing and it has been included in this figure as the "Gust Vane Truth" signal. The Kalman filter's estimated gust vane position closely matches the true gust vane position. Note that the Kalman filter is completely separate from the controller design process, so the same performance would be observed regardless of whether Controllers 1A, 1B, 2A, or 2B were engaged.

The control system implementation had the ability to enable the Kalman filter independently of the feedforward controllers. As a result, the Kalman filter could be engaged without having to engage the feedforward controller. During testing, this ability was used extensively to confirm the Kalman filter had converged prior to engaging the controller.

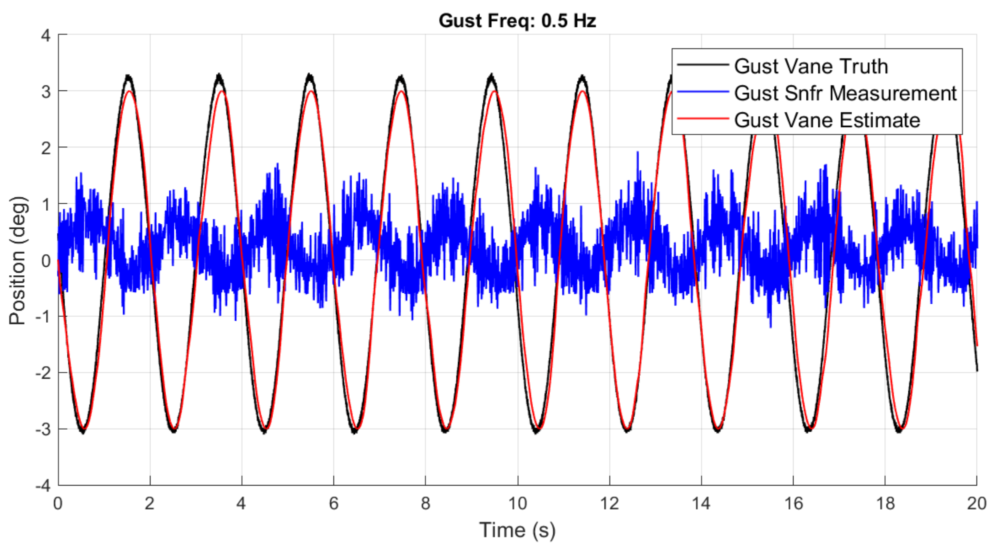

Fig. 19 Extended Kalman filter performance given a 0.5 Hz perturbation of the TDT gust vanes.

Figures 20 - 22 depict the response of Controller 1A with the 0.5 Hz excitation of the gust vanes. The controller is initially disengaged with the system running open-loop until the GLA controller is turned on at roughly t=6 seconds on the plots. The GLA controllers have a 2 second ramp-in time and this transition has been highlighted in the figures. Both the SG01 reading in Figure 20 and the laser displacement reading in Figure 21 show a reduction in the magnitude of the oscillatory response when the controller is engaged. Figure 22 plots the corresponding control surface commands when the GLA controller is engaged. All three aileron commands have similar magnitudes.

For comparison, Figures 23 - 25 depict the response of Controller 2B during a 3.0 Hz excitation of the gust vanes. As previously discussed, Controller 2B disables aileron AILB and the controller is designed for improved higher frequency performance than Controllers 1A/1B. Just as with the previous set of figures, the controller is initially disengaged and running open-loop until the GLA controller is engaged at roughly t=6 seconds. Figures 23 and 24 show a similar reduction in magnitude of the oscillator responses, albeit at the higher frequency. Figure 25 plots the aileron surface commands when the GLA controller is engaged. Unlike the previous case, aileron AILB is zeroed-out. The controller commands noticeably more AILC than AILA to compensate for the effect of the loss of outboard aileron AILB.

A summary of the performance of the 4 controllers is shown in Figures 26 and 27. Figure 26 summarizes the percent reduction on SG01 root-mean-square (RMS) for each of the 4 controllers when compared against the open-loop response. Note that not all of the controllers were tested at each frequency. Figure 27 summarizes the percent reduction of the laser displacement sensor RMS. Controllers 1A and 1B were expected to perform better at the lower frequency range, with the performance tapering off as the gust vane frequency increased. Similarly, it was expected that Controllers 2A

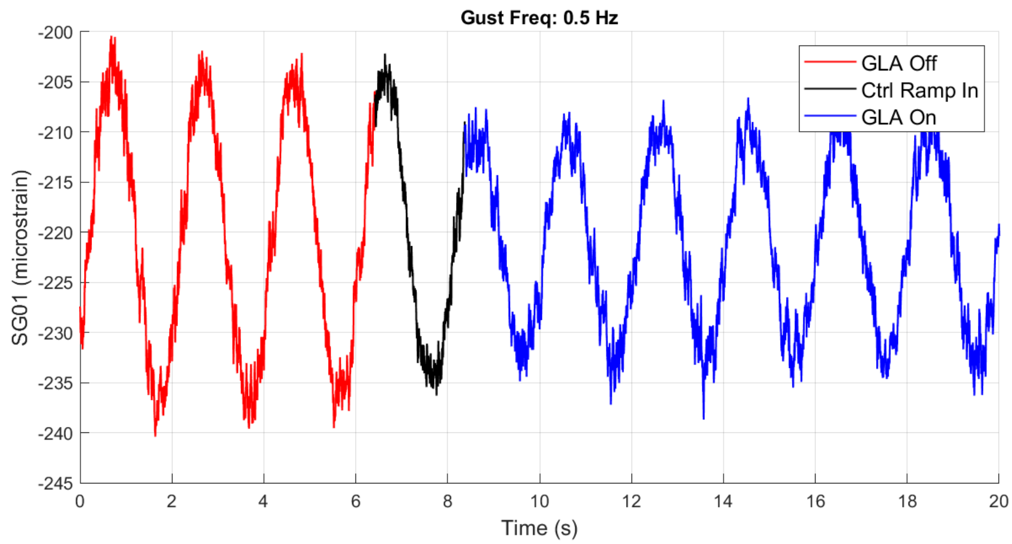

Fig. 20 Strain gage SG01 measurements when GLA Controller 1A is triggered on and off during a 0.5 Hz excitation of the gust vanes.

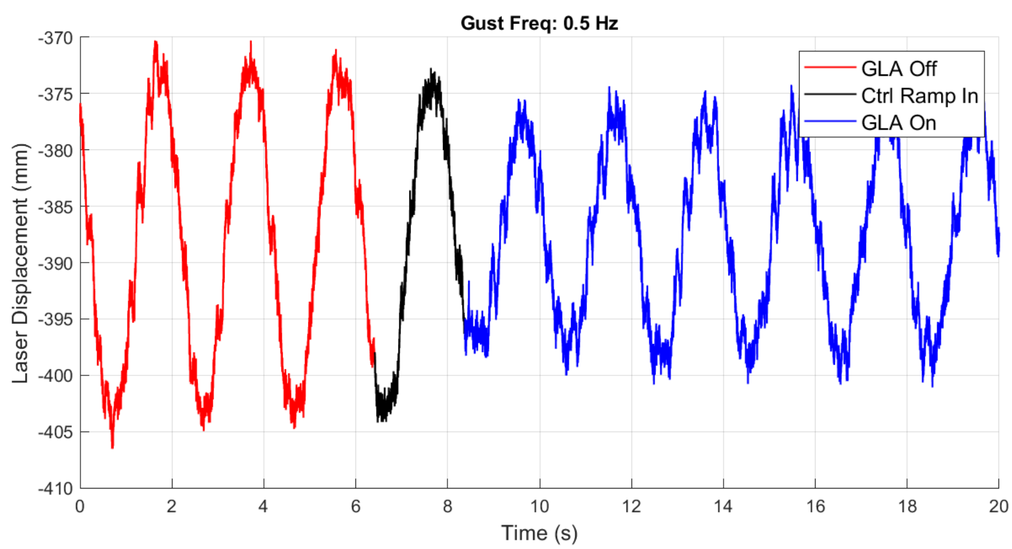

Fig. 21 Laser displacement sensor readings when GLA Controller 1A is triggered on and off during a 0.5 Hz excitation of the gust vanes.

and 2B would perform better at the higher frequency range and worse at the lower frequency values. The experimental data does match these macro trends, although it was not expected for Controllers 2A and 2B to perform so poor at the lower frequency range. Unfortunately, due to test time limitations, there was no time to perform repeat tests at each test condition. Overall, the controllers do demonstrate improvements in wing root bending moment and highlight the potential benefits possible when forward-looking LIDAR sensors are coupled with predictive gust load alleviation control laws.

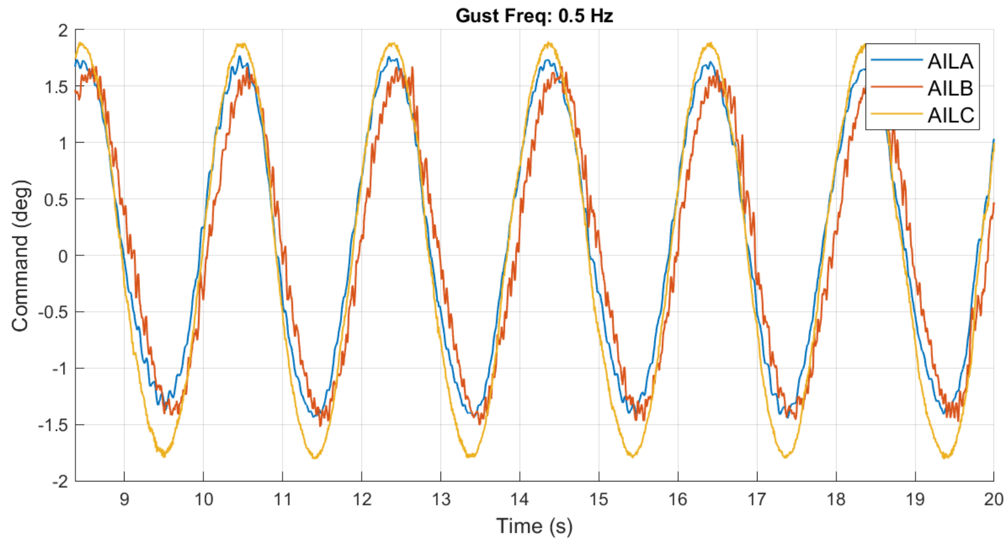

Fig. 22 Aileron control surface commands when GLA Controller 1A is engaged during a 0.5 Hz excitation of the gust vanes.

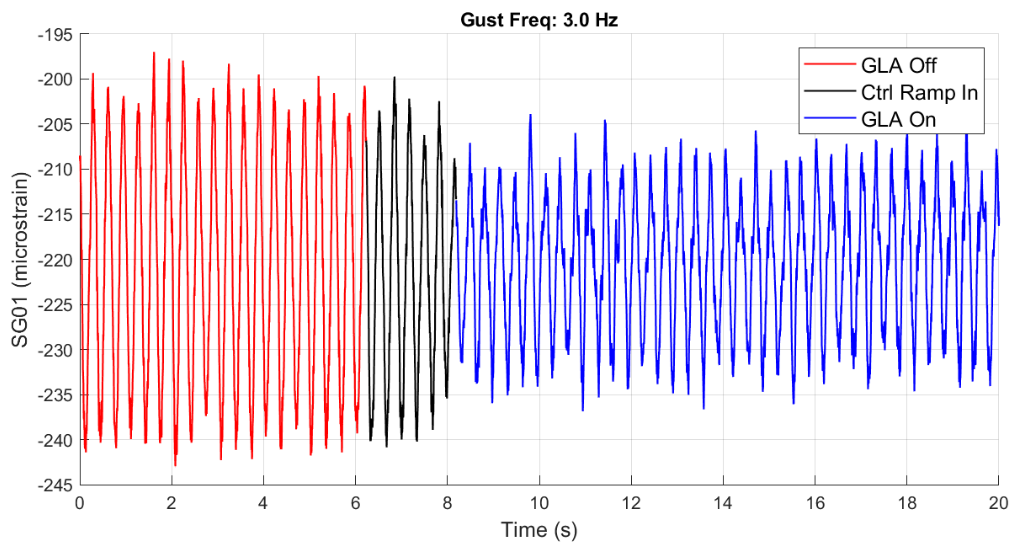

Fig. 23 Strain gage SG01 measurements when GLA Controller 2B is triggered on and off during a 3.0 Hz excitation of the gust vanes.

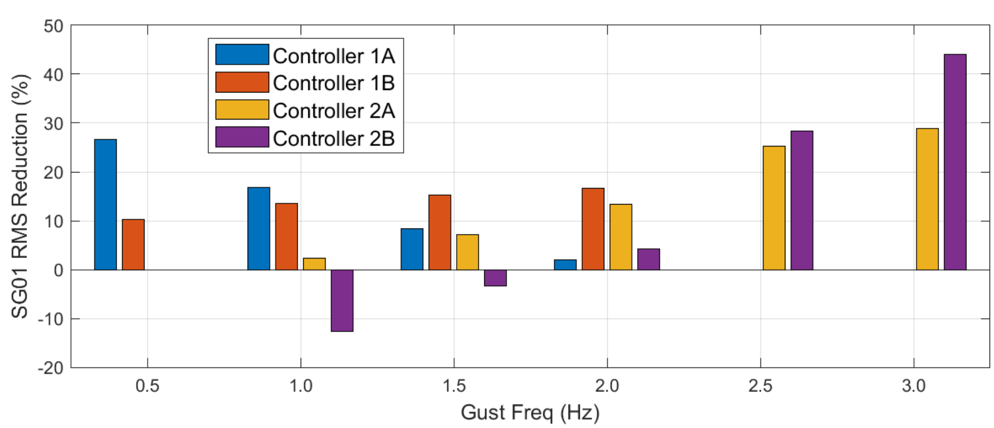

Fig. 26 Summary of the percent reduction of SG01 RMS for each of the 4 controllers tested when compared against the open-loop response.

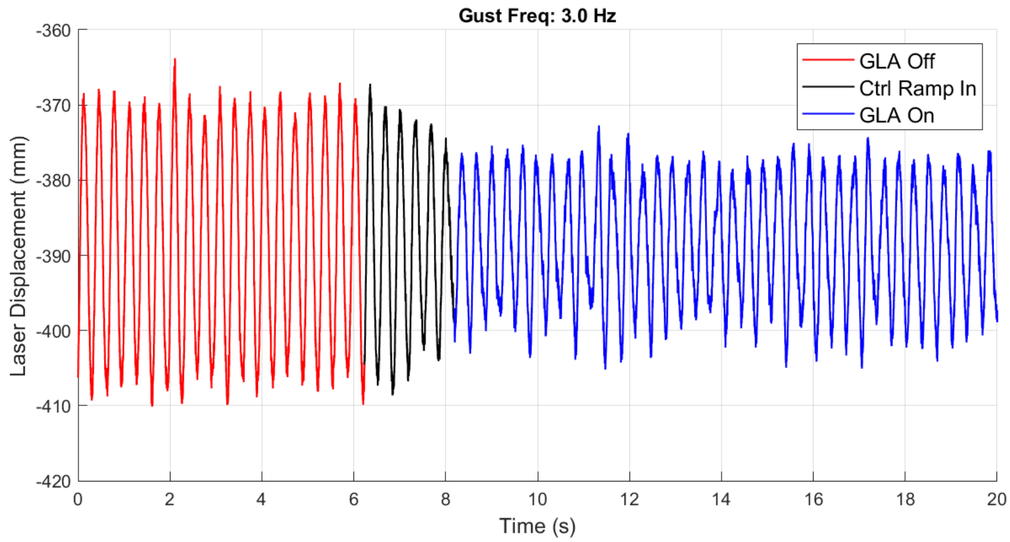

Fig. 24 Laser displacement sensor readings when GLA Controller 2B is triggered on and off during a 3.0 Hz excitation of the gust vanes.

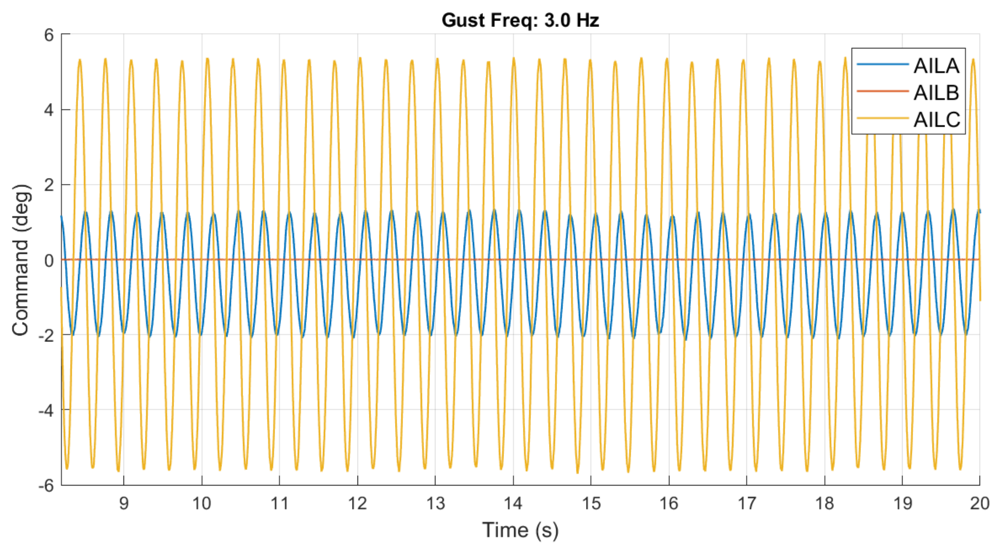

Fig. 25 Aileron control surface commands when GLA Controller 2B is engaged during a 3.0 Hz excitation of the gust vanes.

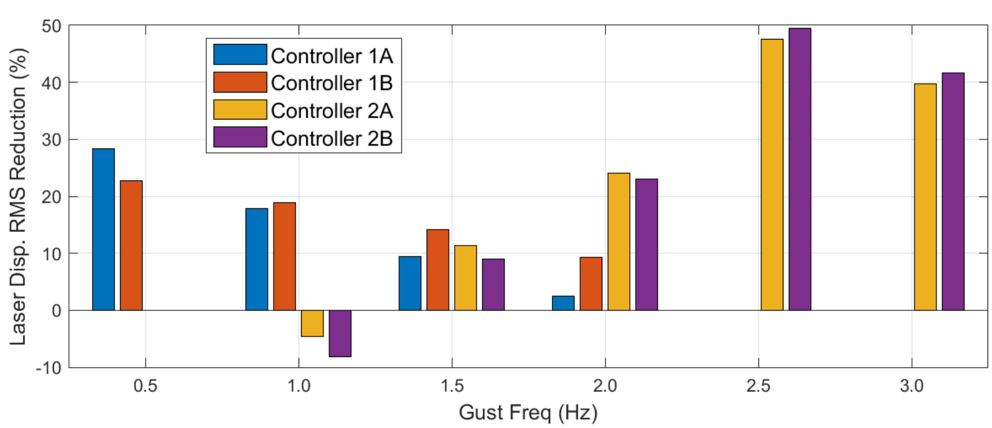

Fig. 27 Summary of the percent reduction of the laser displacement sensor for each of the 4 controller tested when compared against the open-loop response.

B. NASA Ames Results

Closed-loop GLA tests evaluate the performance of two control strategies: the Linear Quadratic Gaussian (LQG) controller and the Hamiltonian-based controller. Both controllers operate at a tunnel condition of Mach 0.55 and a dynamic pressure of $\bar{q}_\infty = 110$ psf. The gust vane is driven at frequencies of 0.5 Hz, 1 Hz, 2 Hz, and 3 Hz. This test series assesses the controllers' effectiveness in attenuating structural responses, particularly root strain, induced by gust disturbances, and compares the performance of different gust estimation schemes.

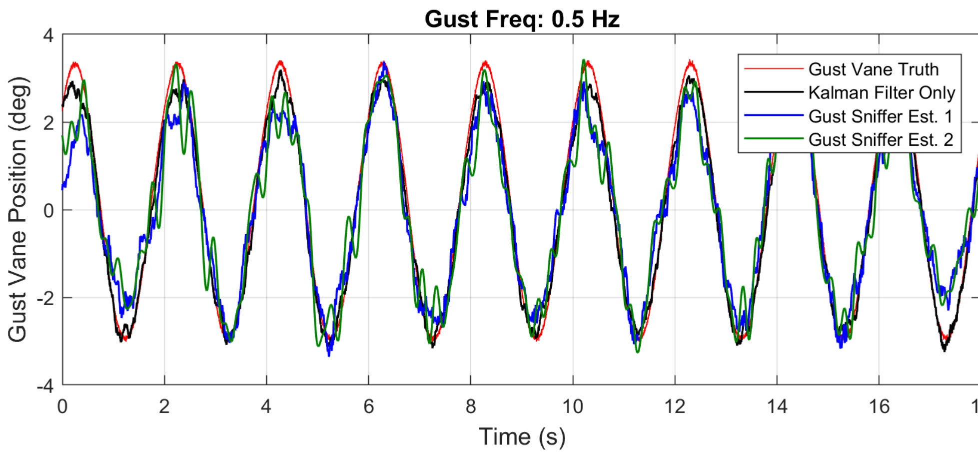

Fig. 28 Gust Estimation Performance for 0.5 Hz AOA Perturbation

Fig. 28 presents the performance of the gust estimation schemes with the controller inactive but the estimation active. Three configurations are examined. The first, labeled *Kalman Filter Only*, uses an extended-state Kalman filter (ESKF) based solely on onboard sensor measurements, without input from the gust sniffer. The second, *Gust Sniffer Est. 1*, incorporates the gust sniffer signal described in Section IV.B.4, with a Kalman filter applied to mitigate measurement noise in the gust sniffer sensor. The third, *Gust Sniffer Est. 2*, employs the same gust sniffer signal but applies a Butterworth low-pass filter instead of a Kalman filter for noise reduction. All three schemes track the gust vane displacement effectively; however, the onboard-only estimation performs slightly better, while *Gust Sniffer Est. 2* appears more susceptible to sensor noise.

Figs. 29-31 show representative results for the LQG controller at 0.5 Hz gust excitation. The plots include the root strain gauge (SG01) measurement, laser displacement measurement, and control surface positions. This controller uses the extended-state Kalman filter estimation scheme. During the test, controller engagement ramps in and out over a 20-second period to minimize transient loads during initial closed-loop testing. Subsequent tests use shorter ramp times once confidence in system stability increases. For this case, response attenuation is visible in both SG01 and laser displacement measurements. The root-mean-square (RMS) values of SG01 and laser displacement reduce by 53.5% and 41.0%, respectively, while control surface activity remains within acceptable limits.

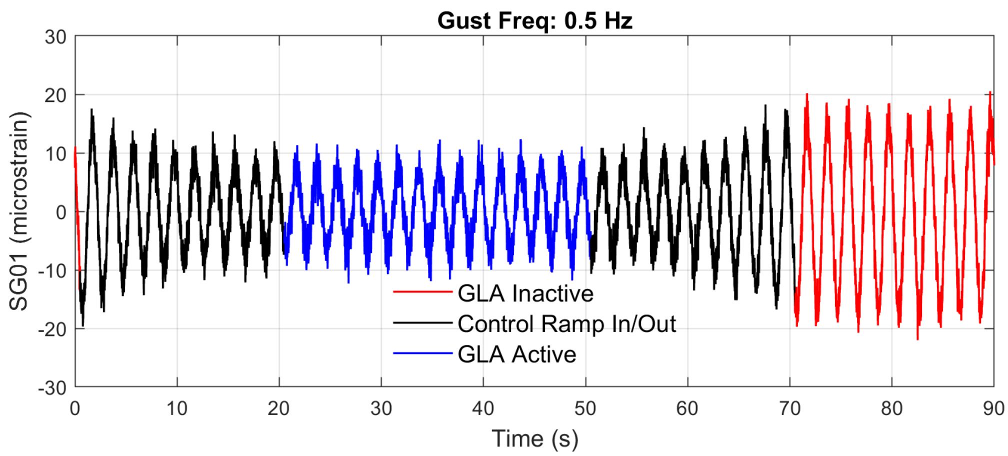

Fig. 29 Root Strain Gauge Measurement for LQG GLA Controller

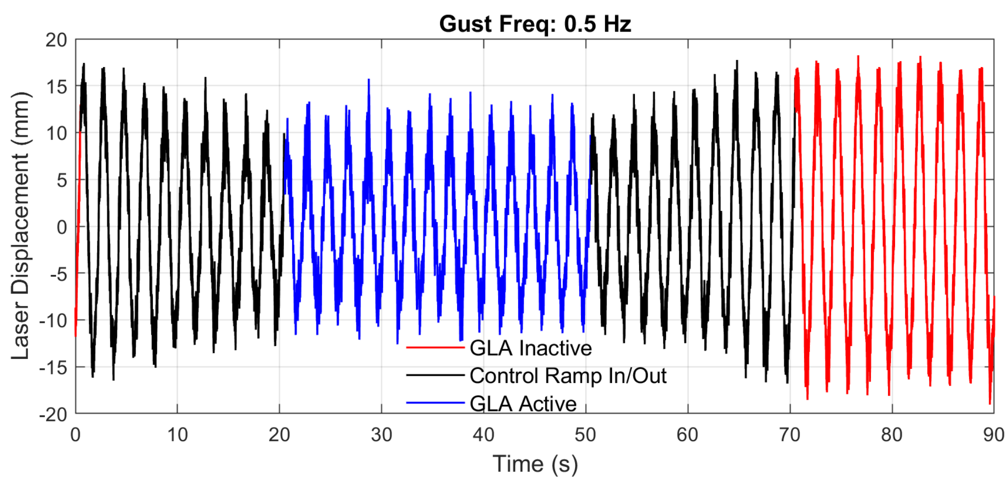

Fig. 30 Tip Laser Displacement Measurement for LQG GLA Controller

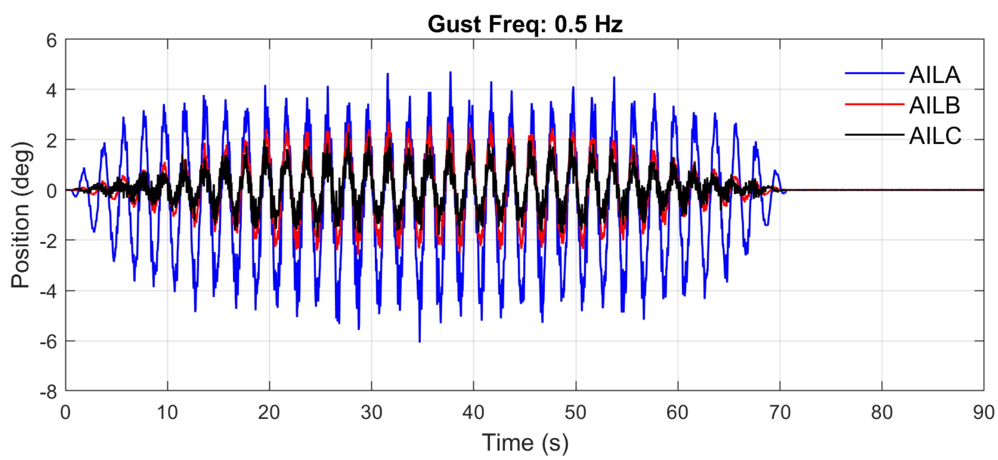

Fig. 31 Control Surface Positions for LQG GLA Controller

Figs. 32-34 present comparable results for the Hamiltonian controller at 0.5 Hz. This controller also uses the extended-state Kalman filter estimation scheme, with a shorter ramp time for control engagement. Attenuation of the response is again observed in both the strain gauge and displacement signals. RMS levels of SG01 and laser displacement reduce by 66.0% and 55.2%, respectively, with control effort remaining reasonable. Notably, the Hamiltonian tests follow the LQG tests, during which the Kalman filter gains are further tuned to improve noise attenuation, reflected in the smoother control surface response.

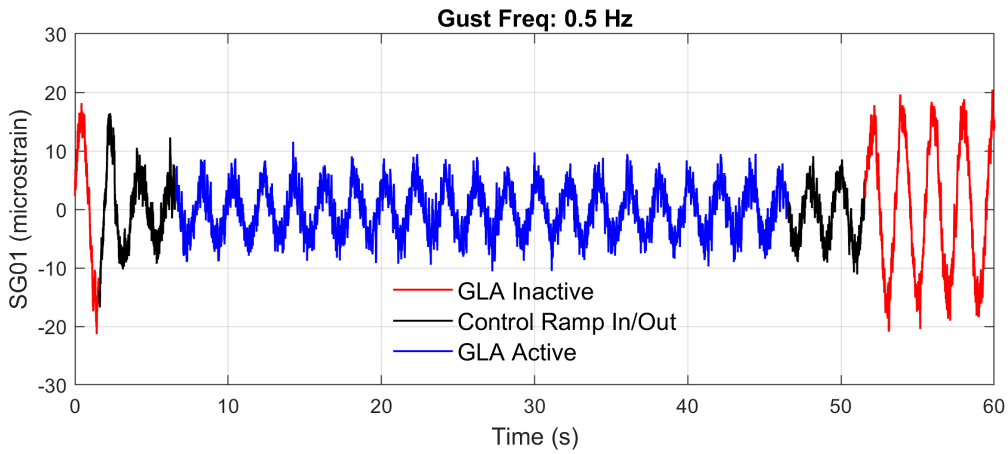

Fig. 32 Root Strain Gauge Measurement for Hamiltonian GLA Controller

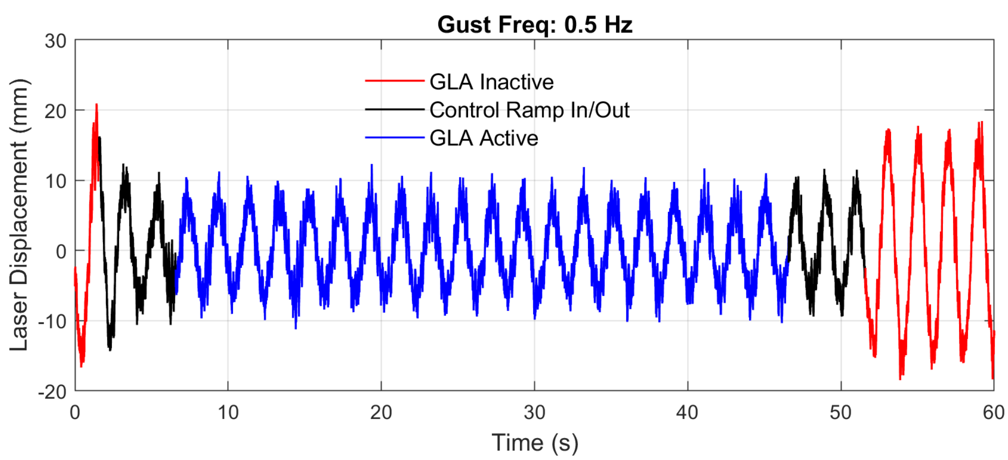

Fig. 33 Tip Laser Displacement Measurement for Hamiltonian GLA Controller

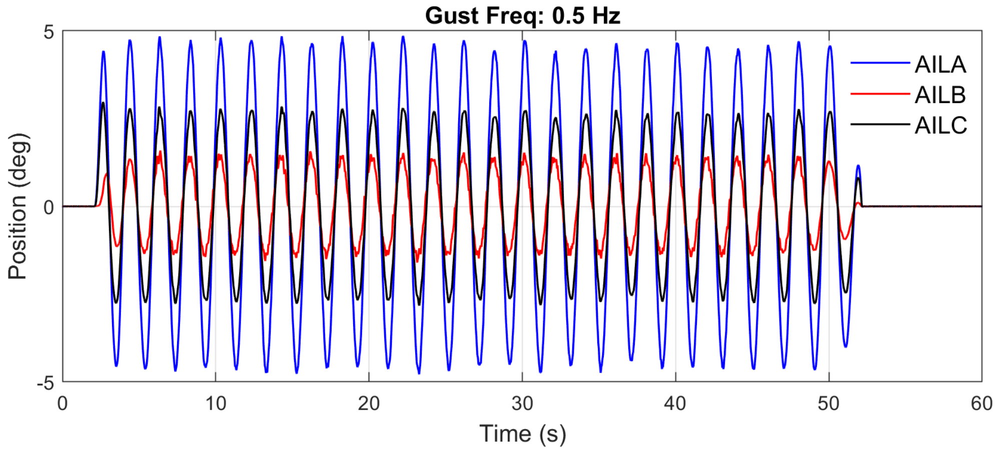

Fig. 34 Control Surface Positions for Hamiltonian GLA Controller

Tab. 6 summarizes test results across all gust frequencies and estimation schemes. Overall, the extended-state Kalman filter provides the most consistent estimation performance for both controllers, while the Hamiltonian-based GLA generally achieves greater response attenuation than the LQG approach. The gust sniffer configurations, though functional, show lower overall performance relative to the onboard-only estimation approach.

Table 6 GLA Performance Summary

Controller	Gust Frequency (Hz)	Estimation Scheme	%SG01 Reduction	% Laser Disp. Reduction
LQG	0.5	Extended-State KF	53.5	41.0
LQG	0.5	Gust Sniffer Est. 1	37.0	20.0
LQG	0.5	Gust Sniffer Est. 2	32.7	15.9
LQG	1	Extended-State KF	53.2	41.7
LQG	1	Gust Sniffer Est. 1	36.7	19.1
LQG	1	Gust Sniffer Est. 2	34.7	17.1
LQG	2	Extended-State KF	52.6	43.8
LQG	2	Gust Sniffer Est. 1	39.5	24.0
LQG	2	Gust Sniffer Est. 2	35.5	18.2
LQG	3	Extended-State KF	55.2	52.9
LQG	3	Gust Sniffer Est. 1	44.2	35.5
LQG	3	Gust Sniffer Est. 2	43.1	31.9
LQG (No AILB)	3	Extended-State KF	55.2	46.2
LQG (No AILB)	3	Gust Sniffer Est. 1	46.4	32.7
LQG (No AILB)	3	Gust Sniffer Est. 2	44.5	30.1
Ham.	0.5	Extended-State KF	66.0	55.2
Ham.	1	Extended-State KF	66.3	56.3
Ham.	2	Extended-State KF	48.5	40.3
Ham.	3	Extended-State KF	57.3	55.1

VI. Conclusion

This paper summarized the development and testing of GLA control laws for the IAWTM wind tunnel test campaign conducted at NASA's Langley Research Center Transonic Dynamics Tunnel in June-July 2025. Both Boeing and NASA developed multiple control laws under the broader IAWTM program that aims to demonstrate key control and sensing technology enablers for higher aspect ratio flexible transport aircraft. In particular, these GLA control laws incorporated the TDT's upstream gust sniffer sensor to act as a surrogate LIDAR for emerging forward-looking gust sensing that can be used to predictively reduce wing root strain. Wind tunnel tests in the TDT have demonstrated various levels of improvement in wing strain measurements with the different NASA and Boeing controllers.

VII. Acknowledgments

This work was supported by the NASA Advanced Air Transport Technology (AATT) Project and the Advanced Air Vehicles Program (AAVP) as part of a Cooperative Agreement with Boeing. The authors would like to acknowledge significant contributions to this project and the work presented in this paper over the course of many years by team members from Boeing, NextGen Aeronautics, and NASA.

References

[1] Brooks, T. R., Kenway, G. K. W., and Martins, J. R. R. A., "Benchmark Aerostructural Models for the Study of Transonic Aircraft Wings," *AIAA Journal*, Vol. 56, No. 7, 2018, pp. 2840–2855. https://doi.org/https://doi.org/10.2514/1.J056603.

[2] Heaney, P. S., and Quindlen, J. F., "Overview of the Integrated Adaptive Wing Technology Maturation Wind-Tunnel Test Objectives," *AIAA SciTech Forum*, Orlando, FL, 2024. https://doi.org/https://doi.org/10.2514/6.2024-2509.

[3] Vassberg, J., Dehaan, M., Rivers, M., and Wahls, R., "Development of a Common Research Model for Applied CFD Validation Studies," *26th AIAA Applied Aerodynamics Conference*, Honolulu, HI, 2008. https://doi.org/https://doi.org/10.2514/6.2008-6919.

[4] Nguyen, N., and Xiong, J., "Real-Time Drag Optimization of Aspect Ratio 13.5 Common Research Model with Distributed Flap System," *AIAA SciTech Forum*, 2021. https://doi.org/https://doi.org/10.2514/6.2021-0069.

[5] Zhao, Y., Yue, C., and Hu, H., "Gust Load Alleviation on a Large Transport Airplane," *Journal of Aircraft*, Vol. 53, No. 6, 2016. https://doi.org/https://doi.org/10.2514/1.C033713.

[6] Fonte, F., Ricci, S., and Mantegazza, P., "Gust Load Alleviation for a Regional Aircraft Through a Static Output Feedback," *Journal of Aircraft*, Vol. 52, No. 5, 2015. https://doi.org/https://doi.org/10.2514/1.C032995.

[7] Regan, C. D., and Jutte, C. V., "Survey of Applications of Active Control Technology for Gust Alleviation and New Challenges for Lighter-weight Aircraft," Tech. rep., NASA, 2012.

[8] Rabadan, G. J., Schmitt, N. P., Pistner, T., and Rehm, W., "Airborne Lidar for Automatic Feedforward Control of Turbulent In-Flight Phenomena," *Journal of Aircraft*, Vol. 47, No. 2, 2010. https://doi.org/https://doi.org/10.2514/1.44950.

[9] Zeng, J., Moulin, B., de Callafon, R., and Brenner, M. J., "Adaptive Feedforward Control for Gust Load Alleviation," *Journal of Guidance, Control, and Dynamics*, Vol. 33, No. 3, 2010. https://doi.org/https://doi.org/10.2514/1.46091.

[10] Fezans, N., and Joos, H.-D., "Combined Feedback and LIDAR-Based Feedforward Active Load Alleviation," *AIAA AVIATION Forum*, Denver, CO, 2017. https://doi.org/https://doi.org/10.2514/6.2017-3548.

[11] Giesseler, H.-G., Kopf, M., Faulwasser, T., Varutti, P., and Findeisen, R., "Model Predictive Control for Gust Load Alleviation," *4th IFAC Nonlinear Model Predictive Control Conference*, Noordwijkerhout, NL, 2012.

[12] Quindlen, J. F., Ortega, D. M., Clark, G. J., Hussain, H. S., Forte, C. J., Nguyen, N. T., Xiong, J., Heaney, P. S., Bentley, P. J., Coulson, D. A., Giles, I. M., McHugh, G. R., Pinkerton, J. L., Ramey, J. M., and Stevens, W. L., "Summary of the Integrated Adaptive Wing Technology Maturation Wind Tunnel Tests of a High Aspect Ratio Commercial Transport Aircraft," *AIAA SciTech Forum*, Orlando, FL, 2026.

[13] Waite, J., Bartels, R. E., and Stanford, B., "Aeroelastic Model Development for the Integrated Adaptive Wing Technology Maturation Project Wind-Tunnel Test," *AIAA AVIATION Forum*, 2020. https://doi.org/https://doi.org/10.2514/6.2020-2717.

[14] Ouellette, J. A., "Updating High-Order Aeroservoelastic Models From Low-Order System Identification Results," *AIAA SciTech Forum*, Orlando, FL, 2025. https://doi.org/https://doi.org/10.2514/6.2025-0463.

[15] Xiong, J., Nguyen, N. T., Stanford, B., and Bartels, R. E., "Aeroelastic Modeling and CFD Simulation of Wind-Tunnel Scale Aspect Ratio 13.5 Common Research Model," *AIAA SciTech Forum*, 2021. https://doi.org/https://doi.org/10.2514/6.2021-2527.

[16] Xiong, J., and Nguyen, N. T., "Aeroelastic Simulation of Wind Tunnel Scale Aspect Ratio 13.5 Common Research Model with Trailing Edge Mini-Flaps," *AIAA SciTech Forum*, Orlando, FL, 2024. https://doi.org/https://doi.org/10.2514/6.2024-2678.

[17] Waite, J. M., Grauer, J., Bartels, R. E., and Stanford, B. K., "Aeroservoelastic Control Law Development for the IntegratedAdaptive Wing Technology Maturation Wind-Tunnel Test," *AIAA SciTech Forum*, 2021. https://doi.org/https://doi.org/10.2514/6.2021-0609.

[18] Bartels, R. E., and Chwalowski, P., "Computational Fluid Dynamics Simulations of the Transonic Dynamics Tunnel Airstream Oscillators," *AIAA SciTech Forum*, 2021. https://doi.org/https://doi.org/10.2514/6.2021-0835.

[19] Nguyen, N. T., and Hashemi, K. E., "Multi-Objective Flight Control for Ride Quality Improvement for Flexible Aircraft," *AIAA SciTech Forum*, 2020. https://doi.org/https://doi.org/10.2514/6.2020-1623.

[20] Forte, C., and Nguyen, N., "Gust Load Alleviation Control and Gust Estimation for a High Aspect Ratio Wing Wind Tunnel Model," *AIAA SciTech Forum*, National Harbor, MD, 2023. https://doi.org/https://doi.org/10.2514/6.2023-0881.

[21] Forte, C., and Nguyen, N., "Multi-Objective Optimal Control of High Aspect Ratio Wing Wind Tunnel Model," *AIAA SciTech Forum*, Orlando, FL, 2024. https://doi.org/https://doi.org/10.2514/6.2024-1782.

[22] Forte, C., and Nguyen, N., "Design and Experimental Validation of Multi-Objective Gust Load Alleviation Optimal Control for a High Aspect Ratio Flexible Transport Wing," *AIAA SciTech Forum*, Orlando, FL, 2026.

[23] Nguyen, N. T., Kelley E. Hashemi, E. A., and Yucelen, T., "Model-Reference Adaptive Control of Distributed Lagrangian Infinite-Dimensional Systems Using Hamilton's Principle," *AIAA SciTech Forum*, 2020. https://doi.org/https://doi.org/10.2514/6.2020-0840.

[24] Nguyen, N., "Distributed Hamiltonian Control of Flexible Aircraft with Adaptive Gust Rejection," *AIAA Scitech Forum*, Orlando, FL, 2024. https://doi.org/https://doi.org/10.2514/6.2024-1784.

[25] Nguyen, N., "Distributed Hamiltonian Adaptive Disturbance Rejection Control with Actuator Dynamics," *AIAA SciTech Forum*, Orlando, FL, 2025. https://doi.org/https://doi.org/10.2514/6.2025-2801.

[26] Forte, C., and Nguyen, N., "Design and Experimental Validation of Hamiltonian Control for Gust Load Alleviation and Flutter Suppression of a High Aspect Ratio Flexible Transport Wing," *AIAA SciTech Forum*, Orlando, FL, 2026.